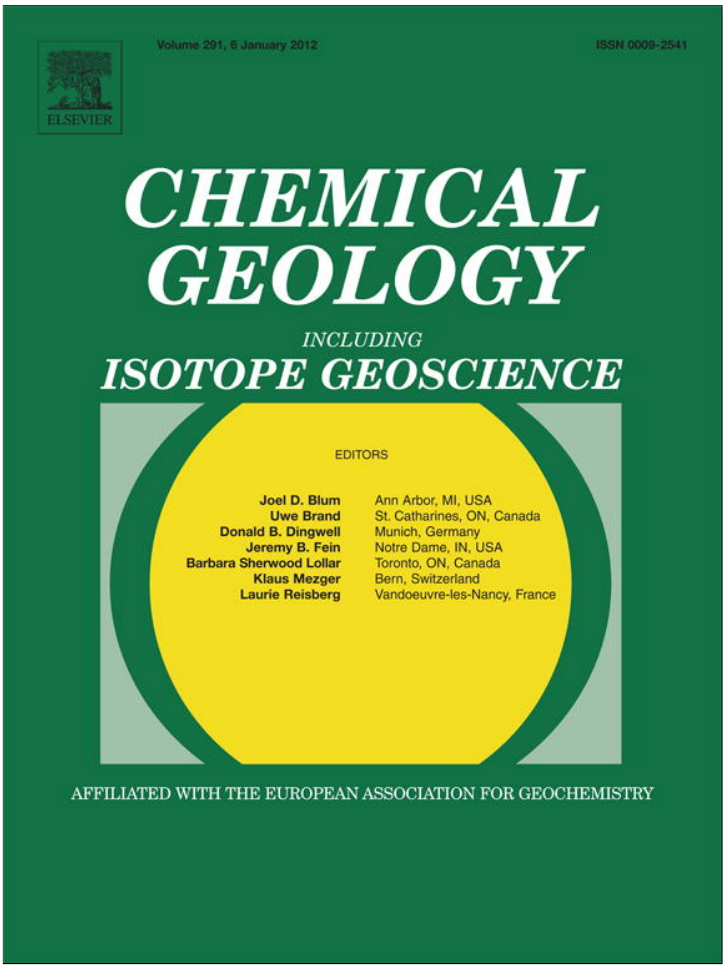

(This is a sample cover image for this issue. The actual cover is not yet available at this time.)

Chemical Geology 306-307 (2012) 40–53

Contents lists available at SciVerse ScienceDirect

Chemical Geology

journal homepage: www.elsevier.com/locate/chemgeo

Research paper

Age, geochemical characteristics and petrogenesis of Late Cenozoic intraplate alkali basalts in the Lut–Sistan region, eastern Iran

Kwan-Nang Pang [a,*], Sun-Lin Chung [a,**], Mohammad Hossein Zarrinkoub [b], Seyyed Saeid Mohammadi [b], Hsiao-Ming Yang [a], Chiu-Hong Chu [a], Hao-Yang Lee [a], Ching-Hua Lo [a]

[a] Department of Geosciences, National Taiwan University, Taipei P.O. Box 13-318, Taipei 106, Taiwan
[b] Department of Geology, Birjand University, Birjand, Iran

ARTICLE INFO

Article history:
Received 18 October 2011
Received in revised form 19 January 2012
Accepted 25 February 2012
Available online 3 March 2012

Editor: D.B. Dingwell

Keywords:
Alkali basalt
$^{40}Ar/^{39}Ar$ dating
Iran
Lut
Sistan
Sr–Nd isotopes

ABSTRACT

Miocene to Quaternary alkali basalts in the Lut–Sistan region, eastern Iran are spatially associated with two active, N–S-trending dextral strike–slip fault systems in the region, i.e., the Neh faults in the Sistan suture zone and the Nayband fault ~200 km further to the west in the Lut block. Here, we present new $^{40}Ar/^{39}Ar$ ages, geochemical and Sr–Nd isotopic data for these rocks to decipher the petrogenetic processes responsible for their formation and regional tectonic implications. Our new ages indicate that the volcanism commenced at ~14 Ma in the western Lut region and ~11 Ma in the northern Sistan suture zone. The rocks are composed dominantly of hawaiites and mugearites with minor basanites and basaltic andesites. Petrographic observations and major and trace elemental variations suggest that the alkali basalts underwent variable fractionation of olivine, clinopyroxene and Fe–Ti oxides. Chondrite-normalized rare earth element and mantle-normalized trace element patterns of these rocks largely resemble those of ocean island basalts. High εNd (t) (+1.4 to +3.6), low to moderate initial Sr isotopic ratios (0.7047–0.7073), and trace element ratios indicate that crustal contamination was insignificant in the petrogenesis. The rocks have neither geochemical features pointing to residual hornblende or phlogopite, nor arc-related signatures characteristic of the Iranian sub-continental lithospheric mantle. Thus, the alkali basalts most likely have asthenospheric origin. Modeling of REE suggests that they could have formed by low degrees of partial melting (~3–10%) of an enriched mantle source at garnet-stable depths. We propose that the east Iranian alkali basaltic volcanism was triggered by asthenospheric upwelling in an extensional setting, presumably caused by delamination of thickened lithospheric root following the Late Cretaceous collision between the Lut and Afghan continental blocks. Our results imply that two contrasting tectonic regimes coexist in Iran since the Middle Miocene, i.e., extensional in eastern and compressional in southwestern Iran.

1. Introduction

Continental intraplate basaltic volcanism has been the subject of intense geochemical investigations, including those on large flood basalt provinces and relatively small volcanic fields. Magmas erupted in these settings are geochemically similar to ocean island basalts (OIB). The huge magma productivity associated with continental flood basalt provinces is commonly attributed to mantle plumes, i.e. hot, actively upwelling asthenosphere from the lower mantle (White and McKenzie, 1989; Campbell and Griffiths, 1990). However, the source and mechanism for the volumetrically minor basaltic volcanism in intra-continental settings are subjected to considerable debate. Proposed models for magma genesis advocate lithospheric mantle origin (Späth et al., 2001; Weinstein et al., 2006; Ma et al., 2011b), asthenospheric origin (Aldanmaz et al., 2000, 2006), or a combination of both (Hoang and Flower, 1998; Johnson et al., 2005; Ma et al., 2011a). The trigger for small-scale intraplate basaltic volcanism has been ascribed to various processes including localized diapirs in the upper mantle (Wilson and Patterson, 2001), adiabatic upwelling related to rifting and extension (McKenzie and Bickle, 1988), lithospheric thinning (Houseman et al., 1981; Houseman and Molnar, 1997), lithospheric delamination (Bird, 1979) or slab detachment (Davies and von Blanckenburg, 1995).

In the Lut–Sistan region, eastern Iran, widespread Eocene–Oligocene calc-alkaline volcanic activity was followed by volumetrically minor, alkali basaltic volcanism from the Miocene to Quaternary. The alkali basaltic volcanism resulted in a series of lava plateaux and small outcrops of lava flows mainly along the Neh and Nayband faults, two active N–S-trending strike–slip fault systems in the region (Fig. 1). The Neh faults are located within the Sistan suture zone, which marks the collision between the Lut and Afghan continental

* Corresponding author. Tel.: +886 2 33662924; fax: +886 2 23636095.
** Corresponding author. Tel.: +886 2 83691242; fax: +886 2 23636095.
E-mail addresses: knpang@ntu.edu.tw (K.-N. Pang), sunlin@ntu.edu.tw (S.-L. Chung).

0009-2541/$ – see front matter © 2012 Elsevier B.V. All rights reserved.
doi:10.1016/j.chemgeo.2012.02.020

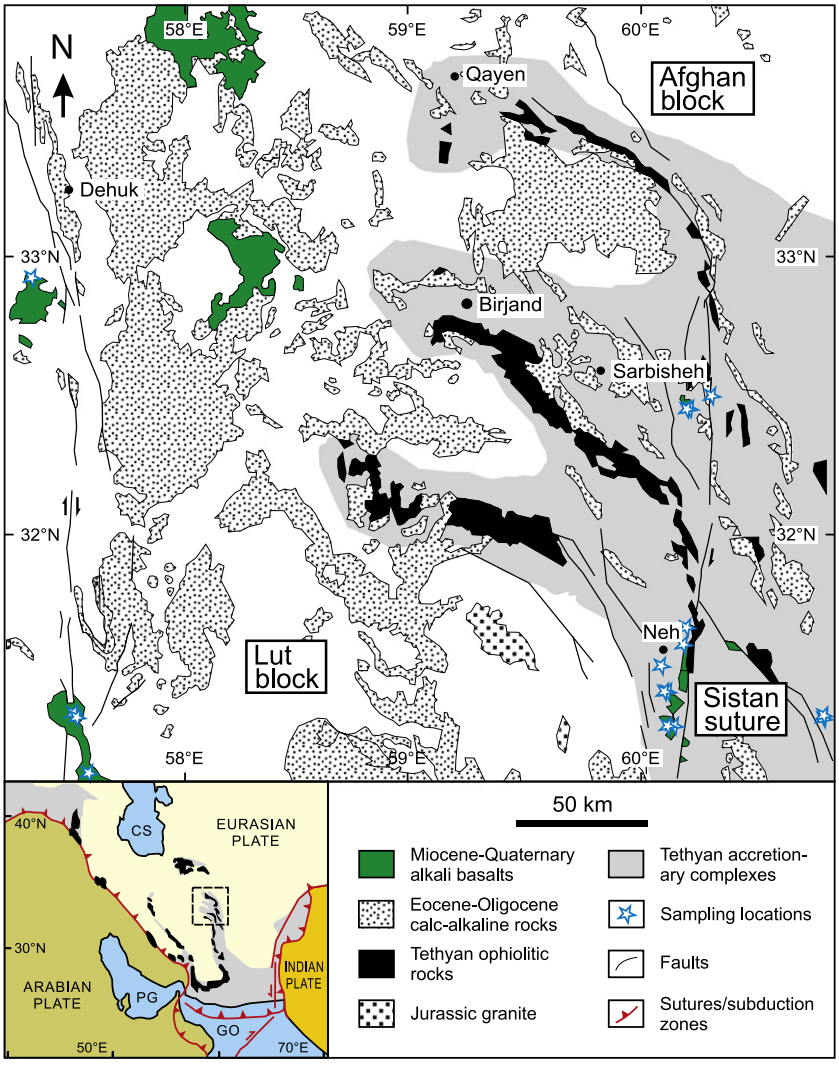

Fig. 1. Geological sketch map of the northern Sistan suture zone, eastern Iran, showing the sampling locations in the Lut–Sistan region. Inset shows the location of the study area in eastern Iran (area bounded by dashed line) and the distribution of major Tethyan ophiolitic rocks. CS = Caspian Sea, PG = Persian Gulf, GO = Gulf of Oman.

blocks presumably at the Late Cretaceous (Zarrinkoub et al., 2010). The east Iranian alkali basalts had only received limited attention following several regional studies in the 1980s (Conrad et al., 1981; Camp and Griffis, 1982; Jung et al., 1983). More recently, Walker et al. (2009) reported some $^{40}Ar/^{39}Ar$ ages and geochemical data for these rocks but the focus of their study was active faulting in the region. In a study of Late Cenozoic alkali basalts in the western Lut region, Saadat et al. (2010) argued that they formed by low and variable degrees of mantle melting, which decrease with time since ~15 Ma. However, this conclusion is based on a limited dataset and how applicable is the model to alkali basalts elsewhere in eastern Iran is uncertain. Thus, it appears that a systematic geochemical study of these rocks is necessary to constrain their petrogenesis and the tectonic evolution of eastern Iran.

In this study, we present new $^{40}Ar/^{39}Ar$ ages, major and trace elemental, and Sr–Nd isotopic data for Late Cenozoic alkali basalts in the Lut–Sistan region, eastern Iran. The data provide new insights into: (i) the onset of alkali basaltic volcanism and its tectonic implications, (ii) the geochemical features of the mantle source involved in alkali basalt genesis, (iii) the controls of magma generation processes, and (iv) the probable effects of low-pressure processes such as fractional crystallization and crustal contamination. Using the new dataset, we demonstrate that the east Iranian alkali basalts are low-degree partial melts from the convecting upper mantle that erupted since ~14 Ma in an extensional setting.

2. Geological background

Iran represents part of the Alpine–Himalayan orogenic system and consists of various microcontinental blocks separated by narrow belts of Mesozoic ophiolitic rocks (Şengör et al., 1988; Ghazi et al., 2004). Despite a complex tectonic history from the Permian to Quaternary, most regions of the country is underlain by Paleozoic platform strata similar to those of the Arabian platform (Stöcklin, 1968). The microcontinental blocks are therefore suggested to share a common paleogeographic position close to the northern margin of Gondwanaland (Ramezani and Tucker, 2003), rifted in successive stages and were accreted to the southern margin of Eurasia (Şengör and Natal'in, 1996).

Iran consists of three orogenic belts juxtaposed with major suture zones and magmatic belts; these belts surround an assembly of continental blocks collectively known as the central Iranian micro-continent (CIM), consisting of the Lut, Tabas and Yazd blocks from east to west. The CIM is suggested to have undergone anti-clockwise rotation from the Late Cretaceous to Early Tertiary (Conrad et al., 1981; Shafiei et al., 2009). The Alborz–Kopeh Dagh ranges are associated with a Paleotethyan suture in northern Iran (Alavi et al., 1997) and magmatic rocks,

mostly Eocene–Oligocene in age, crop out to the south of and roughly parallel to the suture. The Zagros fold and thrust belt and the Bitlis–Zagros suture in southwestern Iran mark the closure of Neotethys and the collision between the Afro–Arabian continent and Eurasia. The collision is interpreted by different workers to have started in the Late Eocene (Allen and Armstrong, 2008; Hatzfeld and Molnar, 2010), the Late Oligocene (Allen et al., 2004; Agard et al., 2005; Fakhari et al., 2008), or the Miocene (McQuarrie et al., 2003; Verdel et al., 2007). The Sanandaj–Sirjan zone (SSZ) and the Urumieh–Dokhtar magmatic arc (UDMA), both of which are roughly parallel to the Zagros orogen, are manifestations of the prolonged subduction of Tethyan oceanic lithosphere beneath the Eurasian continental margin prior to the Arabia–Eurasia collision. The SSZ consists mostly of metamorphic rocks with minor Mesozoic intrusions while the UDMA is dominated by Eocene–Oligocene volcanic rocks. Post-collisional magmatic rocks along the UDMA include ultrapotassic volcanic rocks (Ahmadzadeh et al., 2010), kamafugitic rocks (Pang et al., 2011), and adakitic rocks (Jahangiri, 2007; Omrani et al., 2008). The east Iranian ranges and the Sistan suture zone mark the closure of the Sistan Ocean, a narrow branch of Neotethys that opened during the Middle Cretaceous (Camp and Griffis, 1982; Tirrul et al., 1983). This was accompanied by the suturing between the Lut block and the Afghan block to the east at the Late Cretaceous (Saccani et al., 2010; Zarrinkoub et al., 2010). Magmatism for the Lut block was active from the Jurassic to Quaternary with a dominant pulse during the Eocene–Oligocene (see Karimpour et al., 2011 for review), which resulted in calc-alkaline rocks covering a region of at least ~300×400 km^2. The N–S-trending Nayband fault separating the Lut and Tabas blocks appears to be the westernmost boundary for this rock suite.

The Late Cenozoic alkali basalts crop out along the Neh faults in the Sistan suture zone and the Nayband fault in the western Lut region, eastern Iran. The faults represent two active, N–S-trending dextral strike–slip fault systems separated by a distance of ~200 km largely covered by a desert (i.e. Dasht-e–Lut) (Wellman, 1966; Walker and Jackson, 2002). In general, the alkali basalts occur as lava plateaux ranging in size from a few to some 10 km across (Fig. 2a) and small outcrops that are probably remnants of originally larger plateaux. The lava sequences exhibit columnar jointing perpendicular to the flow tops in places (Fig. 2b). Limited data for these rocks along the Neh faults indicate that they are composed of mugearites and hawaiites (Walker et al., 2009). Those along the Nayband fault include basanites and basaltic andesites in addition to the above rock types (Jung et al., 1983; Saadat et al., 2010). The basanites are reported from Gandum Beryan, a major lava plateau along the central Nayband fault. Several volcanic cones occur along the fault trace and Jung et al. (1983) noted the occurrence of mantle xenoliths in this locality. The basaltic andesites crop out further north near the town of Tabas. Limited K–Ar and ^{40}Ar/^{39}Ar ages suggest that the volcanism was active from ~15.5 to ~1.6 Ma (Conrad et al., 1981; Camp and Griffis, 1982; Jung et al., 1983; Walker et al., 2009). Besides, Walker et al. (2009) also reported an ^{40}Ar/^{39}Ar age of ~27 Ma for a trachyandesite collected along the West Neh fault, but its relation to the alkali basalts is hitherto not clear.

3. Sample description and petrography

Fourteen samples of alkali basalts were collected from outcrops in the Lut–Sistan region, eastern Iran. Additional 6 samples of similar lithology were obtained from Walker et al. (2009) for Sr–Nd isotopic analyses. The rocks are characterized by a mineral assemblage of olivine (~10–30%), clinopyroxene (~5–10%), plagioclase (~45–55%) and Fe–Ti oxides (~4–6%). They are generally fresh and exhibit either porphyritic or aphyric textures. Olivine phenocrysts are the most common but clinopyroxene and plagioclase phenocrysts, and microphenocrysts of Fe–Ti oxides are present (Fig. 2c and d). Glomeroporphyritic aggregates of olivine and plagioclase are observed in places. The phenocrysts occur in a microlitic to glassy groundmass of the same mineralogy. Replacement of olivine by iddingsite (Fig. 2d) and

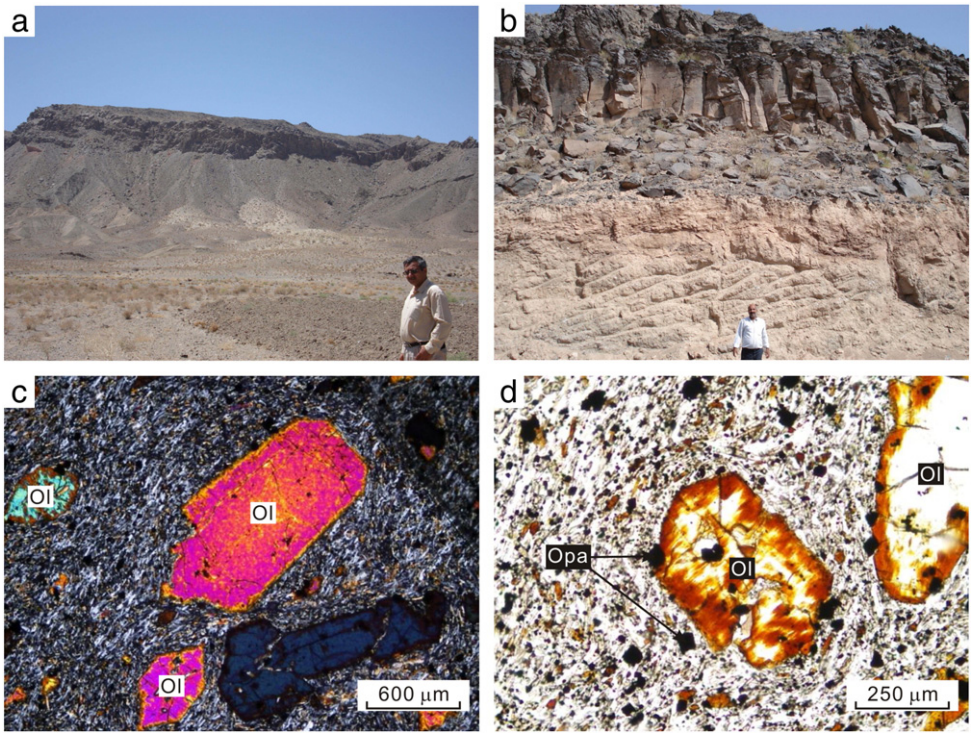

Fig. 2. Field occurrence and thin section textures of the Late Cenozoic alkali basalts, eastern Iran. a. Lava flows of alkali basalts (top of hill) east of Nehbandan. b. Columnar jointing perpendicular to the top of an alkali basalt flow (top of view), Solabest Road. c. Euhedral olivine (Ol) phenocrysts in a microlitic groundmass of olivine, clinopyroxene, plagioclase and Fe–Ti oxides (Opa) in alkali basalt (crossed polars). d. Olivine phenocrysts and Fe–Ti oxide micro-phenocrysts in the same microlitic groundmass as Fig. 2c (plane-polarized light); the olivine phenocrysts are surrounded by iddingsite rims.

Table 1
$^{40}Ar/^{39}Ar$ dating results for the Late Cenozoic alkali basalts, eastern Iran.

T (°C)	Cum. $^{39}Ar_K$ (%)	Atmos.[a]	$^{36}Ar/^{39}Ar$	$^{37}Ar/^{39}Ar$	$^{38}Ar/^{39}Ar$	$^{40}Ar/^{39}Ar$	$^{40}Ar/^{36}Ar$	Age (Ma ± 1σ)[b]
Sample Z-50-85								
600	0.003	98.670	2.39E-01	1.76E+00	6.11E-02	7.14E+01	2.99E+02	6.5 ± 1.8
700	0.017	94.525	8.56E-02	1.10E+00	3.04E-02	2.67E+01	3.12E+02	10.1 ± 0.4
800	0.069	90.916	5.66E-02	8.23E-01	2.40E-02	1.84E+01	3.24E+02	11.5 ± 0.4
900	0.218	83.684	2.88E-02	8.15E-01	1.82E-02	1.01E+01	3.52E+02	11.4 ± 0.3
950	0.392	76.987	1.90E-02	7.85E-01	1.64E-02	7.24E+00	3.81E+02	11.4 ± 0.2
1000	0.541	71.704	1.40E-02	8.38E-01	1.53E-02	5.72E+00	4.08E+02	11.1 ± 0.2
1050	0.634	69.751	1.29E-02	1.16E+00	1.52E-02	5.36E+00	4.16E+02	11.1 ± 0.2
1100	0.689	67.621	1.21E-02	3.12E+00	1.54E-02	4.95E+00	4.11E+02	11.0 ± 0.2
1150	0.830	55.294	7.79E-03	5.80E+00	1.44E-02	3.40E+00	4.37E+02	10.4 ± 0.4
1200	0.907	61.581	9.87E-03	6.01E+00	1.50E-02	4.03E+00	4.08E+02	10.6 ± 0.4
1400	0.964	72.012	1.50E-02	6.55E+00	1.58E-02	5.50E+00	3.67E+02	10.6 ± 0.4
1600	1.000	86.674	3.21E-02	6.59E+00	1.91E-02	1.04E+01	3.24E+02	9.6 ± 0.5
Integrated age = 11.0 ± 0.2 Ma								
Plateau age = 11.0 ± 0.2 Ma (700–1600 °C)						*J*-value[c] = 0.003824114 ± 0.000009207		
Sample Z-B-1-85								
600	0.004	67.733	1.22E-02	9.43E-01	1.89E-02	5.25E+00	4.30E+02	11.6 ± 0.5
700	0.026	36.906	3.22E-03	6.77E-01	1.57E-02	2.47E+00	7.67E+02	10.6 ± 0.2
800	0.097	68.169	1.10E-02	5.67E-01	1.60E-02	4.72E+00	4.30E+02	10.3 ± 0.1
900	0.201	55.912	6.68E-03	5.94E-01	1.49E-02	3.48E+00	5.21E+02	10.5 ± 0.1
950	0.309	52.468	5.71E-03	6.01E-01	1.46E-02	3.16E+00	5.53E+02	10.2 ± 0.1
1000	0.387	46.373	4.51E-03	6.52E-01	1.44E-02	2.80E+00	6.20E+02	10.2 ± 0.1
1050	0.463	45.316	4.37E-03	8.08E-01	1.44E-02	2.75E+00	6.28E+02	10.2 ± 0.1
1100	0.546	35.636	3.11E-03	1.82E+00	1.39E-02	2.22E+00	7.15E+02	9.7 ± 0.2
1150	0.801	23.451	2.26E-03	2.94E+00	1.39E-02	1.93E+00	8.55E+02	10.0 ± 0.2
1200	0.896	40.373	4.10E-03	3.03E+00	1.42E-02	2.47E+00	6.01E+02	10.0 ± 0.2
1400	0.963	77.198	1.81E-02	3.11E+00	1.66E-02	6.66E+00	3.68E+02	10.4 ± 0.2
1600	1.000	88.510	3.68E-02	3.06E+00	2.02E-02	1.21E+01	3.28E+02	9.5 ± 0.4
Integrated age = 10.1 ± 0.2 Ma								
Plateau age = 10.1 ± 0.1 Ma (600–1600 °C)						*J*-value = 0.003824114 ± 0.000009207		
Sample Z-BKH-1								
600	0.001	>100	1.45E-01	1.26E+00	4.10E-02	3.36E+01	2.32E+02	−77.9 ± 6.7
700	0.006	99.176	3.95E-02	1.75E+00	2.12E-02	1.17E+01	2.95E+02	0.8 ± 0.5
800	0.021	96.773	1.64E-02	1.44E+00	1.49E-02	4.94E+00	3.00E+02	1.3 ± 0.5
850	0.055	87.164	7.91E-03	1.36E+00	1.35E-02	2.59E+00	3.28E+02	2.7 ± 0.2
900	0.117	67.023	3.69E-03	1.14E+00	1.29E-02	1.53E+00	4.14E+02	4.1 ± 0.2
950	0.208	57.438	2.69E-03	1.01E+00	1.29E-02	1.28E+00	4.76E+02	4.4 ± 0.2
1000	0.336	78.521	6.33E-03	8.78E-01	1.35E-02	2.33E+00	3.68E+02	4.1 ± 0.2
1050	0.486	70.866	4.63E-03	8.97E-01	1.33E-02	1.86E+00	4.03E+02	4.4 ± 0.2
1100	0.605	68.842	4.17E-03	9.77E-01	1.32E-02	1.71E+00	4.11E+02	4.3 ± 0.2
1150	0.691	73.526	4.73E-03	1.09E+00	1.34E-02	1.82E+00	3.84E+02	3.9 ± 0.2
1200	0.757	71.527	5.59E-03	1.22E+00	1.37E-02	2.21E+00	3.95E+02	5.1 ± 0.2
1300	0.831	73.356	7.58E-03	1.42E+00	1.42E-02	2.94E+00	3.87E+02	6.4 ± 0.2
1450	0.929	71.818	1.40E-02	1.33E+00	1.57E-02	5.63E+00	4.04E+02	13.0 ± 0.2
1500	1.000	73.064	1.95E-02	1.23E+00	1.69E-02	7.80E+00	3.99E+02	17.2 ± 0.2
Integrated age = 6.0 ± 0.2 Ma								
Plateau age = 4.23 ± 0.14 Ma (900–1150 °C)						*J*-value = 0.004578220 ± 0.000001749		
Sample 08-06								
600	0.076	83.421	3.10E-02	4.24E-01	1.95E-02	1.10E+01	3.54E+02	14.5 ± 0.3
700	0.223	80.574	2.56E-02	9.02E-01	1.85E-02	9.32E+00	3.65E+02	14.4 ± 0.2
800	0.383	77.371	2.19E-02	1.38E+00	1.76E-02	8.24E+00	3.77E+02	14.8 ± 0.2
850	0.526	77.405	2.12E-02	1.78E+00	1.75E-02	7.94E+00	3.75E+02	14.3 ± 0.2
900	0.631	77.407	2.13E-02	2.39E+00	1.74E-02	7.92E+00	3.72E+02	14.2 ± 0.3
950	0.730	77.915	2.18E-02	3.33E+00	1.74E-02	7.98E+00	3.66E+02	14.0 ± 0.3
1000	0.796	78.539	2.27E-02	4.39E+00	1.74E-02	8.14E+00	3.59E+02	13.9 ± 0.5
1050	0.838	80.839	2.54E-02	5.97E+00	1.77E-02	8.76E+00	3.45E+02	13.4 ± 0.4
1100	0.867	81.285	2.85E-02	9.17E+00	1.79E-02	9.55E+00	3.35E+02	14.3 ± 0.7
1150	0.898	82.463	2.91E-02	8.99E+00	1.85E-02	9.62E+00	3.31E+02	13.5 ± 0.6
1200	0.934	82.348	2.93E-02	8.48E+00	1.86E-02	9.75E+00	3.33E+02	13.8 ± 0.6
1300	0.971	83.035	3.43E-02	8.94E+00	1.95E-02	1.14E+01	3.33E+02	15.5 ± 0.9
1450	0.989	93.866	1.04E-01	9.08E+00	3.20E-02	3.21E+01	3.08E+02	15.8 ± 1.5
1500	1.000	97.660	3.14E-01	8.94E+00	6.94E-02	9.43E+01	3.01E+02	17.7 ± 1.2
Integrated age = 14.4 ± 0.2 Ma								
Plateau age = 14.3 ± 0.2 Ma (600–1200 °C)						*J*-value = 0.004439595 ± 0.000015893		

[a] Atmos. (%) = $[1 - {}^{40}Ar^*/({}^{40}Ar^* + {}^{40}Ar_{air})] \times 100$, * = radiogenic ^{40}Ar.

[b] Age = $(1/\lambda)$ ln $[1 + (J \times {}^{40}Ar^*/{}^{39}Ar_K)]$ and ${}^{40}Ar^*/{}^{39}Ar_K = \{[{}^{40}Ar/{}^{39}Ar]_m - 295.5 \times [{}^{36}Ar/{}^{39}Ar]_m + 295.5 \times [{}^{36}Ar/{}^{37}Ar]_{Ca} \times [{}^{37}Ar/{}^{39}Ar]_m\}/\{1 - [{}^{39}Ar/{}^{37}Ar]_{Ca} \times [{}^{37}Ar/{}^{39}Ar]_m\} - [{}^{40}Ar/{}^{39}Ar]_K$ where λ = decay constant from Steiger and Jäger (1977), $[]_{Ca}$ and $[]_K$ = isotope ratios of argon extracted from irradiated Ca and K salts and $[]_m$ = isotope ratio of argon extracted from irradiated unknown.

[c] *J*-value = neutron flux calculated using Ar compositions of the biotite standard LP-6 (128.5 ± 0.5 Ma) and calibrated by Fish Canyon sanidine (28.03 ± 0.08 Ma) (Jourdan and Renne, 2007).

chlorite, and of clinopyroxene by chlorite, is observed in places. Amygdules filled with calcite and gypsum are also noted.

4. Analytical methods

The samples were carefully cut into rock chips, some of which were crushed after removal of weathering rinds. They were pulverized in agate mortars to minimize potential contamination of transition metals in trace element analyses. The resultant rock powders were used for whole-rock geochemical and Sr–Nd isotopic analyses. The remaining rock chips were used for $^{40}Ar/^{39}Ar$ dating.

4.1. $^{40}Ar/^{39}Ar$ geochronology

Four samples were dated by $^{40}Ar/^{39}Ar$ step-heating technique. The rock chips were crushed and sieved to sizes of 425–850 μm, ultrasonically cleaned in distilled water and dried, and then handpicked to remove any visible impurities. The samples were then irradiated together with the biotite standard LP-6 in the VT-C position at the THOR Reactor at Taiwan (Lo et al., 2002). After irradiation, the standard and samples were degassed using a double-vacuum resistance furnace in steps from 600 to 1600 °C with a 30-min heating schedule or using a defocused Nd-YAG laser system (US LASER) in steps by increasing energy. Furnace temperatures were calibrated to ±2 °C. Argon isotopes were measured using Varian-MAT GD150 and VG3600 mass spectrometers at Department of Geosciences, National Taiwan University, Taiwan. Isotopic results were corrected for mass discrimination, interfering nuclear reactions, procedural blanks and atmospheric Ar contamination. Detailed analytical procedures were described in Lo et al. (2002) and Lee et al. (2009).

4.2. Major and trace element analyses

Loss-on-ignition (LOI) and abundances of major and trace elements were determined at Department of Geosciences, National Taiwan University, Taiwan. LOI was obtained by routine procedures. Major element oxides were measured on fused glass disks using a Rigaku® RIX 2000 X-ray fluorescence (XRF) spectrometer. Concentrations of trace elements were determined by inductively coupled plasma-mass spectrometry (ICP-MS) using an Agilent 7500s machine, following the analytical procedures of Lee et al. (2011). Standard additions were used to establish absolute abundance and pure elemental standards were used for external calibration. Analytical uncertainties were estimated to be better than 5% (relative) for the XRF analyses and 3% (relative) for the ICP-MS analyses.

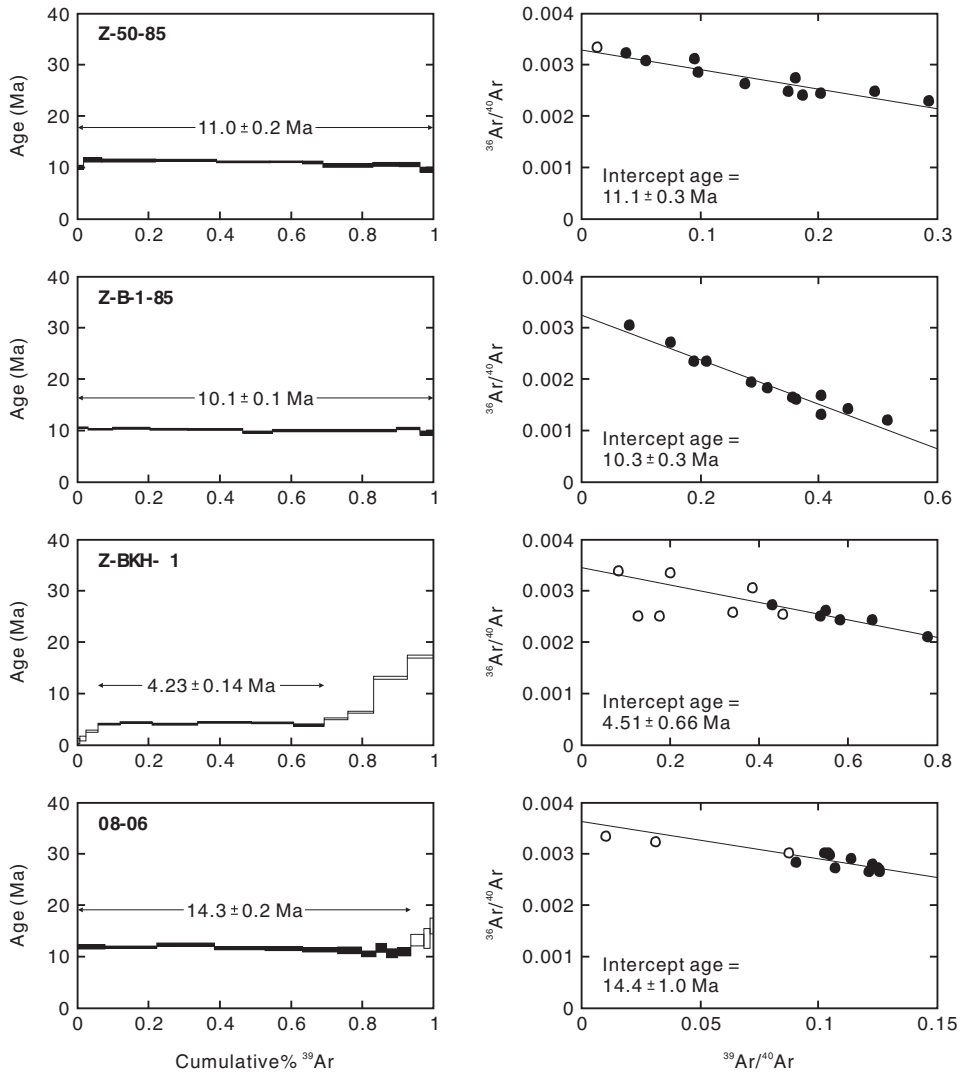

Fig. 3. Apparent age spectra and $^{36}Ar/^{40}Ar$–$^{39}Ar/^{40}Ar$ diagrams of step-heating analyses for selected Late Cenozoic alkali basalts, eastern Iran. Plateau ages were calculated using the steps between arrows in the age spectra. The vertical height of each step, shown as black horizontal bar, represents 2σ analytical errors. Empty circles in the $^{36}Ar/^{40}Ar$–$^{39}Ar/^{40}Ar$ diagrams were not used for age calculation.

4.3. Sr–Nd isotopic analyses

The samples were analyzed for Sr–Nd isotopes at Department of Geosciences, National Taiwan University, Taiwan. Chemical separation of Sr and Nd was performed using routine cation-exchange column techniques after repeated digestion by HF–HNO_3 mixtures in closed Teflon beakers. Isotopic ratios $^{87}Sr/^{86}Sr$ and $^{143}Nd/^{144}Nd$ were determined by a Thermo Finnigan Neptune multi-collector ICP-MS. Detailed analytical procedures follow Lee et al. (2011). Within-run isotopic fractionation was corrected for $^{88}Sr/^{86}Sr = 8.375209$ and $^{146}Nd/^{144}Nd = 0.7219$. Repeated measurements of standards SRM987 and JNdi-1 during the course of the analyses yield $^{87}Sr/^{86}Sr$ of 0.710271 ± 12 ($n = 8$) and $^{143}Nd/^{144}Nd$ of 0.512120 ± 11 ($n = 4$), respectively.

5. Results

5.1. $^{40}Ar/^{39}Ar$ dating results

The Ar isotopic data and calculated ages for the samples are listed in Table 1. $^{40}Ar/^{39}Ar$ step-heating analyses for samples Z-50-85, Z-B-1-85 and 08-06 yield flat age spectra of 11.0 ± 0.2, 10.1 ± 0.1 and 14.3 ± 0.2 Ma, respectively (Fig. 3). In $^{36}Ar/^{40}Ar$–$^{39}Ar/^{40}Ar$ diagrams, the data for these samples define linear arrays with reasonable values of the mean square of the weighted deviates (MSWD; 1.25–1.82). The intercept ages are consistent with the plateau ages for each individual sample (Table 1). The age spectrum of sample Z-BKH-1 shows minor disturbance, probably due to alteration (Fig. 3). As a result, its plateau

Table 2
Major and trace element data for the Late Cenozoic alkali basalts, eastern Iran.

Sample	Z-50-85	Z-B-1-85	Z-B-2-85	Z-BKH-1	Z-BKH-2	08-06	08-07	08-112	09-09	09-10	10-08	10-10	10-14	10-14 (dup)
Lat. E	32°29′ 30″	32°27′ 25″	32°26′ 42″	31°36′ 20″	31°40′ 24″	32°57′ 09″	32°57′ 09″	31°01′ 56″	31°20′ 08″	31°20′ 00″	31°32′ 21″	31°26′ 25″	29°58′ 47″	
Long. N	60°19′ 34″	60°12′ 43″	60°13′ 58″	60°11′ 53″	60°12′ 32″	57°20′ 27″	57°20′ 27″	61°29′ 13″	60°53′ 00″	60°52′ 56″	60°06′ 24″	60°07′ 05″	60°50′ 38″	
Major oxides (wt.%)														
SiO_2	45.15	47.34	47.41	48.08	52.87	54.46	54.80	48.84	56.98	54.47	54.43	52.69	48.13	
TiO_2	3.22	2.89	2.59	2.44	1.59	1.83	1.86	2.25	1.44	1.45	1.65	1.90	1.90	
Al_2O_3	13.73	13.63	14.21	14.95	16.09	15.52	15.67	15.85	17.07	16.49	16.33	15.07	15.96	
Fe_2O_3[a]	12.49	11.35	10.55	9.64	6.48	9.89	9.90	9.73	5.80	5.93	6.34	7.78	9.18	
MnO	0.16	0.16	0.14	0.13	0.11	0.12	0.14	0.14	0.08	0.08	0.09	0.11	0.12	
MgO	8.19	7.50	7.84	5.60	3.73	4.95	4.81	5.82	3.28	3.48	3.64	5.17	6.83	
CaO	8.98	8.35	8.80	9.48	7.31	6.63	6.77	9.06	7.02	8.60	8.35	8.87	9.37	
Na_2O	3.21	3.65	3.68	4.38	5.03	4.32	4.28	5.02	5.40	5.44	5.01	4.39	3.74	
K_2O	1.32	1.88	1.39	1.25	0.97	0.84	1.12	1.24	1.44	1.47	1.59	1.65	1.31	
P_2O_5	0.63	0.64	0.61	1.04	0.80	0.32	0.34	1.10	0.72	0.82	0.87	0.98	0.54	
LOI	2.12	1.37	1.19	1.33	1.40	0.31	0.88	1.31	1.36	1.42	1.78	0.86	4.21	
Total	99.19	98.77	98.40	98.31	96.38	99.20	100.56	100.35	100.58	99.66	100.08	99.46	101.29	
Mg#[b]	57.9	58.1	60.9	54.9	54.7	51.2	50.5	55.7	54.3	55.2	54.7	58.2	60.9	
Trace elements (ppm)														
Sc	20.7	16.2	16.7	17.3	10.6	46.1	46.2	30.5	25.5	22.8	10.2	13.7	20.4	14.9
V	269	228	222	245	115	119	120	190	111	114	103	148	187	175
Cr	207	196	240	113	67.6	241	175	99.5	114	140	56.0	191	294	270
Co	44.1	35.2	34.7	33.3	19.6	30.6	30.1	30.0	17.2	17.5	17.8	24.8	34.1	32.4
Ni	84.2	90.0	104	76.6	45.3	117	81.5	68.0	54.0	67.5	38.9	103	117	107
Cu	62.7	48.3	40.7	103	54.7	36.3	40.5	75.1	57.1	61.2	47.3	57.1	65.5	62.7
Zn	161	137	124	136	105	92.9	113	164	94.9	90.7	98.8	103	97.7	86.3
Ga	21.9	20.6	19.6	22.2	20.4	21.6	21.9	22.7	20.8	20.2	19.4	19.2	20.6	19.0
Rb	22.7	42.0	26.6	25.4	18.6	29.5	31.9	25.7	21.0	20.8	24.0	29.9	16.0	15.2
Sr	812	870	940	1240	1738	404	721	1144	1051	1519	1098	1809	1230	1171
Y	26.0	24.9	24.1	26.5	17.6	18.9	19.1	24.9	13.9	13.7	15.7	19.3	16.2	14.8
Zr	238	252	213	267	244	138	142	252	216	199	221	227	149	135
Nb	25.7	29.5	26.9	38.1	26.8	22.6	24.3	35.0	17.2	17.8	26.9	29.4	37.7	35.2
Cs	1.00	1.68	1.16	1.43	1.00	0.62	0.63	1.20	1.50	1.21	0.93	1.04	1.73	1.61
Ba	221	316	269	362	354	216	322	324	348	495	404	576	818	775
La	27.9	31.7	28.4	49.9	47.7	12.9	13.8	45.6	36.9	46.4	43.8	52.4	25.2	25.5
Ce	75.5	80.8	68.5	110	95.8	27.3	28.9	105	80.1	97.1	91.6	109	50.7	49.3
Pr	10.6	11.0	9.11	13.6	11.0	3.62	3.82	13.1	9.60	11.3	10.9	13.1	6.42	6.18
Nd	46.8	46.6	39.5	54.0	41.9	16.1	17.1	50.4	35.8	41.2	40.1	48.3	26.3	25.6
Sm	9.55	9.06	8.09	10.0	7.30	4.75	4.88	9.77	6.43	6.95	7.05	8.37	5.74	5.43
Eu	2.48	2.31	2.16	2.64	1.93	1.57	1.64	2.65	1.79	1.95	1.93	2.29	1.98	1.93
Gd	7.91	7.37	6.86	8.19	5.97	4.77	4.88	7.66	4.95	5.24	5.25	6.26	4.80	4.53
Tb	1.13	1.03	0.99	1.14	0.78	0.70	0.72	1.02	0.65	0.68	0.69	0.83	0.66	0.61
Dy	5.46	4.93	4.87	5.27	3.48	3.91	3.95	4.94	2.98	2.93	3.31	3.99	3.36	3.15
Ho	0.95	0.87	0.87	0.93	0.61	0.72	0.72	0.90	0.52	0.52	0.57	0.71	0.62	0.56
Er	2.40	2.16	2.16	2.31	1.50	1.72	1.75	2.15	1.32	1.35	1.40	1.73	1.49	1.36
Tm	0.30	0.28	0.28	0.29	0.19	0.22	0.22	0.27	0.17	0.16	0.17	0.22	0.19	0.17
Yb	1.80	1.67	1.68	1.76	1.13	1.33	1.38	1.68	1.00	1.00	1.04	1.31	1.15	1.04
Lu	0.25	0.24	0.24	0.24	0.16	0.19	0.19	0.21	0.14	0.14	0.15	0.19	0.16	0.15
Hf	5.88	6.10	5.26	5.94	5.12	3.44	3.50	5.28	4.55	4.26	4.60	4.93	3.29	3.04
Ta	1.55	1.81	1.59	2.06	1.33	1.64	1.74	2.19	0.99	1.00	1.39	1.59	2.15	1.99
Pb	3.81	5.60	4.70	7.21	8.07	1.56	2.56	5.49	7.83	9.82	9.62	8.86	2.84	2.79
Th	2.20	3.82	2.79	3.72	5.00	1.71	1.74	3.16	4.09	4.59	5.02	6.61	3.98	3.70
U	0.45	0.71	0.58	0.41	1.23	0.46	0.48	0.53	0.81	1.05	1.25	0.96	0.92	0.85

[a] Total iron as Fe_2O_3.
[b] $Mg\# = [\text{molar } 100 \times Mg/(Mg + Fe^{2+})]$, assuming 15% of total iron oxide is ferric.

age (4.23 ± 0.14 Ma) and integrated age (6.0 ± 0.2 Ma) exhibit a larger difference than the other samples. The intercept age of this sample is 4.51 ± 0.66 Ma with MSWD of 1.1, which is statistically more consistent with its plateau age.

5.2. Major and trace elements

Major and trace element compositions for the samples are listed in Table 2. Except two samples collected from Tabas (08-06 and 08-07), most samples are characterized by high alkalinity index [$(Na_2O + K_2O) - (0.37 \times SiO_2 - 14.43)$] from +0.87 to +2.61. On a total alkalis–SiO_2 diagram, they plot in fields of mugearite and hawaiite with one sample on the boundary between basalt and basanite (Fig. 4a). The two Tabas samples are classified as basaltic andesite. On a Zr/TiO_2–Nb/Y diagram, however, all samples plot in the field of alkali basalt (Fig. 4b).

The SiO_2 concentrations of the alkali basalts range from 45.2 to 57.0 wt.% and, together with published data, correlate negatively with TiO_2 (1.44–3.22 wt.%), Fe_2O_3 (5.80–11.4 wt.%), MgO (3.28–8.19 wt.%), CaO (6.63–9.48 wt.%) and Mg# (50.5–60.9), and positively with Al_2O_3 (13.6–17.1 wt.%) (Figs. 5a–e and 6a). The trends for Na_2O, K_2O and P_2O_5 are less well-defined but there is a tendency for samples relatively rich in SiO_2 to have high Na_2O concentrations (Fig. 5f–h). Most samples contain ~10–30 ppm Sc, except the two Tabas samples having ~46 ppm Sc (Fig. 6b). The V contents of the basalts range from ~100 to 270 ppm and decrease with increasing SiO_2 concentrations, whereas their Cr contents scatter at the same SiO_2 interval (Fig. 6c and d). No systematic trends exist between Sr, Nb, La or Th and SiO_2 in the samples (Fig. 6e–h). Some samples, which are basanites reported by Saadat et al. (2010), have high Nb concentrations of ~80 ppm (Fig. 6f).

Fig. 7 shows the chondrite-normalized rare earth element (REE) and primitive mantle-normalized trace element diagrams for the alkali basalts. Our data are generally consistent with those of Walker et al. (2009) and Saadat et al. (2010) obtained from the same rock suite, except the absence of positive Pr anomaly shown by samples of Walker et al. (2009) (Fig. 7a). Such a feature is extremely rare in igneous rocks and may be related to analytical problems. Except the two Tabas samples, the basalts define a tight envelope with fractionated REE patterns (e.g. La/Yb = 15.5–46.5, Sm/Yb = 4.82–6.97) generally resembling OIB (Fig. 7a). The two Tabas samples display less fractionated REE patterns (e.g. La/Yb = 9.70–10.0, Sm/Yb = 3.53–3.56) compared to other basalts. Primitive mantle-normalized patterns for the basalts are also OIB-like except the presence of slight negative K and positive Sr anomalies (Fig. 7b).

5.3. Sr–Nd isotopes

Sr–Nd isotopic analyses for rocks in this study are listed in Table 3. Ranges for initial Sr isotopic ratios and $\varepsilon Nd(t)$ of the basalts are 0.7047–0.7073 and +1.4 to +3.6, respectively. In a $\varepsilon Nd(t)$–$(^{87}Sr/^{86}Sr)_i$ space, the data plot between end-members of depleted MORB mantle (DMM) or Iranian ophiolites and global subducted sediment (GLOSS) or enriched mantle II (Fig. 8a). The data appear to diverge from a point at about $\varepsilon Nd(t) = +3.5$ and $(^{87}Sr/^{86}Sr)_i = 0.7047$ (Fig. 8b). No systematic variations exist between $(^{87}Sr/^{86}Sr)_i$ and SiO_2 concentrations (Fig. 8c), but samples rich in SiO_2 tend to have low $\varepsilon Nd(t)$ (Fig. 8d).

6. Discussion

6.1. Onset of alkali basaltic volcanism

Existing K–Ar and $^{40}Ar/^{39}Ar$ age data indicate that eruption of alkali basalts in eastern Iran commenced at ~15.5 Ma and were still active by ~1.6 Ma (Conrad et al., 1981; Camp and Griffis, 1982; Jung et al., 1983; Walker et al., 2009). Our new $^{40}Ar/^{39}Ar$ ages provide additional constraints on the duration and continuity of the volcanism. Sample 08-06 taken from Tabas yields plateau and intercept ages of ~14.3 Ma (Fig. 3 and Table 1), slightly younger than the oldest published K–Ar age of ~15 Ma in that region. Samples Z-50-85 and Z-B-1-85 from the northern Sistan suture zone yield ages of ~10–11 Ma (Fig. 3 and Table 1), which are approximately 3 to 4 m.y. older than the oldest published K–Ar age of ~7.3 Ma along the Neh faults. Our new $^{40}Ar/^{39}Ar$ age results indicate that the east Iranian alkali basaltic volcanism initiated at ~14 Ma in the western Lut region and approximately 3 to 4 m.y. later in the northern Sistan suture zone. In addition, the new and published ages indicate that the volcanism was continuous without major magmatic gaps. Our unpublished age and geochemical data for the Late Oligocene trachyandesites (see Walker et al., 2009) indicate that these rocks and the alkali basalts are not cogenetic. These authors concluded that the trachyandesite unit where they sampled was mis-mapped as Plio–Quaternary. If this is true, the trachyandesites may represent the waning stage of the calc-alkaline volcanism that was active from the Eocene to the Oligocene in the Lut–Sistan region.

6.2. Effects of alteration, fractional crystallization and crustal contamination

Most samples are petrographically fresh with only little signs of alteration, reflected in their generally low LOI values (mostly <2 wt.%). No correlation exists between LOI and CaO, Na_2O and K_2O

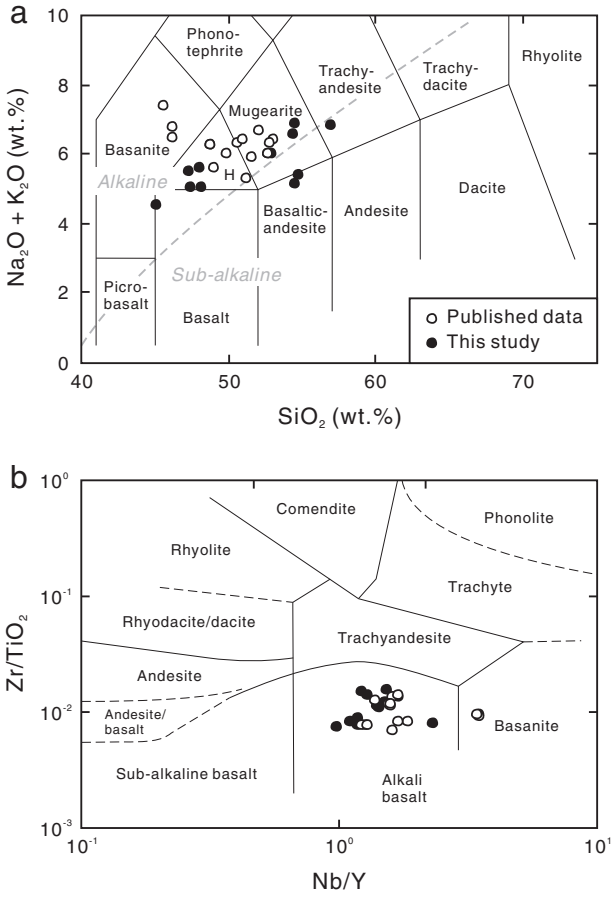

Fig. 4. Discrimination diagrams for the Late Cenozoic alkali basalts, eastern Iran. a. Total alkalis–SiO_2 diagram (after Le Bas et al., 1986 and Le Maitre, 2002); the dashed line separating the sub-alkaline and alkaline fields was after Irvine and Baragar (1971). H = hawaiite. b. Zr/TiO_2–Nb/Y diagram (after Winchester and Floyd, 1977). Published data are after Walker et al. (2009) and Saadat et al. (2010).

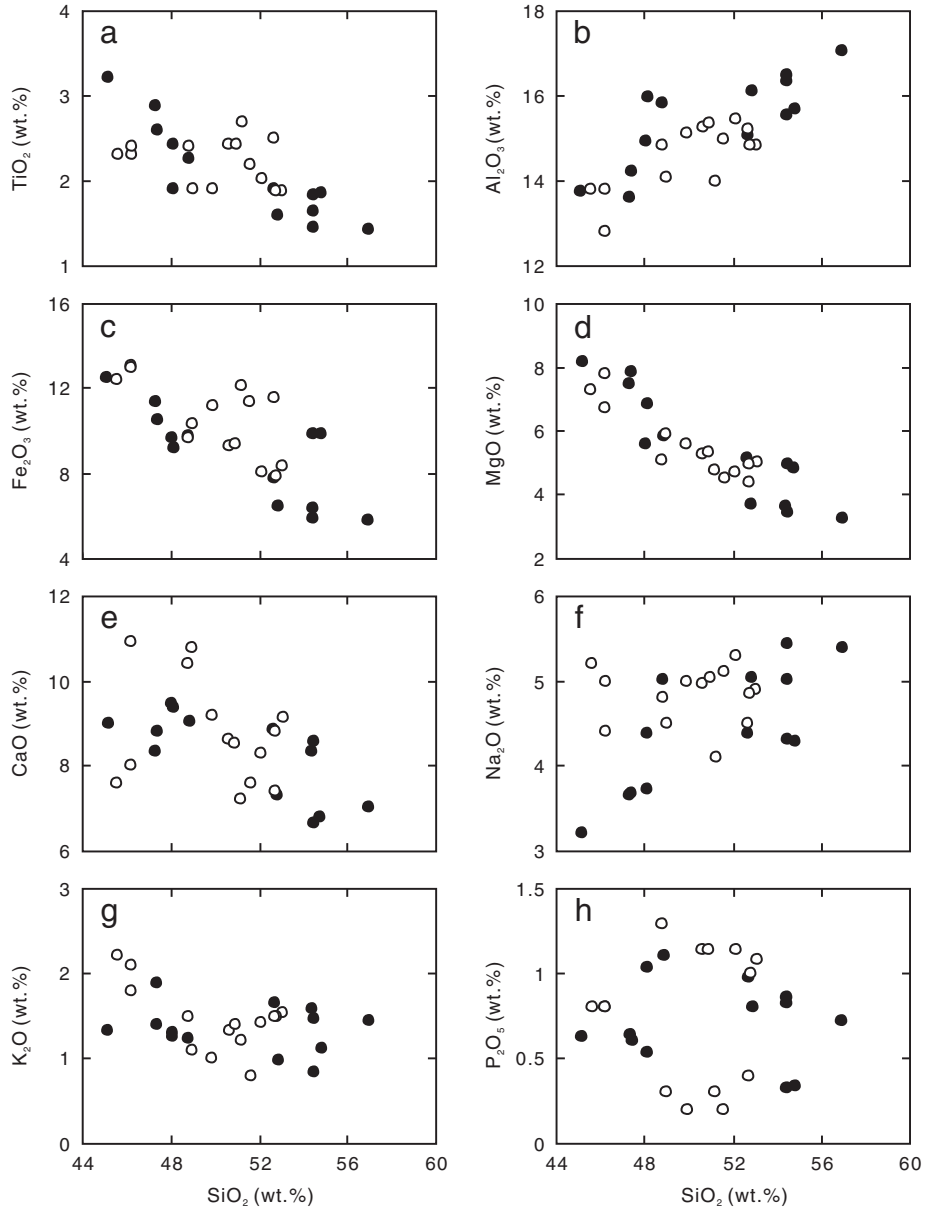

Fig. 5. Concentrations of major element oxides versus SiO_2 for the Late Cenozoic alkali basalts, eastern Iran. a. TiO_2. b. Al_2O_3. c. Total iron as Fe_2O_3. d. MgO. e. CaO. f. Na_2O. g. K_2O. h. P_2O_5. Legend is the same as in Fig. 4.

contents, suggesting that the effects of carbonate and sericite replacement are limited. Likewise, the lack of correlation between LOI and some mobile trace elements (e.g. Cs, Rb, Ba and U) indicates that variations of the latter might not be alteration-related. Generally, abundances of most trace elements of the samples exhibit relatively restricted ranges (Table 2); abnormally low or high contents, as would be expected for extensive alteration, are extremely rare. We suggest, therefore, that the effects of alteration on the east Iranian alkali basalts are negligible.

The alkali basalts in this study have variable MgO (3.28–8.19 wt.%) and Mg# (50.5–60.9) that are substantially lower than would be expected for pristine mantle melts. This, together with the occurrence of olivine, clinopyroxene and plagioclase phenocrysts in the rocks, is consistent with crystal fractionation during magma ascent. Trends of decreasing MgO, CaO, Ni and Cr with increasing SiO_2 (Figs. 5d, e and 6b, d) are consistent with fractionation of olivine, clinopyroxene and probably chrome spinel. Decreases in TiO_2, Fe_2O_3 and V associated with increase in SiO_2 (Figs. 5a, c and 6c) point to fractionation of Fe–Ti oxides. The lack of negative correlations between Y or Sm, elements with relatively high K_D for amphibole-liquid compared to pyroxene-liquid (Rollinson, 1993), and Rb (index of fractionation) suggests that amphibole fractionation was not significant (Fig. 9). Some scatter in Figs. 5 and 6 may represent varying extents of phenocryst accumulation or, alternatively, different degrees of partial melting. Overall, the dominant fractionation assemblage of the alkali basalts is olivine + clinopyroxene + Fe–Ti oxides ± chrome spinel.

Before eruption, the east Iranian alkali basalts had to pass through the continental crust in which potential contamination may occur. Crustal contamination should drive the magma compositions towards high $(^{87}Sr/^{86}Sr)_i$, low $\varepsilon Nd(t)$ and trace element ratios towards average crustal values. The small $\varepsilon Nd(t)$ range defined by the alkali basalts in this study (+1.4 to +3.6) is a strong indicator that extensive assimilation of crustal rocks did not occur. Samples with relatively low $\varepsilon Nd(t)$ in the suite do not have the lowest Nb/La, Ce/Pb and highest Ba/Nb and Th/Nb as expected for crustal contamination (Fig. 10). In particular, their supra-chondritic Nb/La (~1.5–2.0) might have been

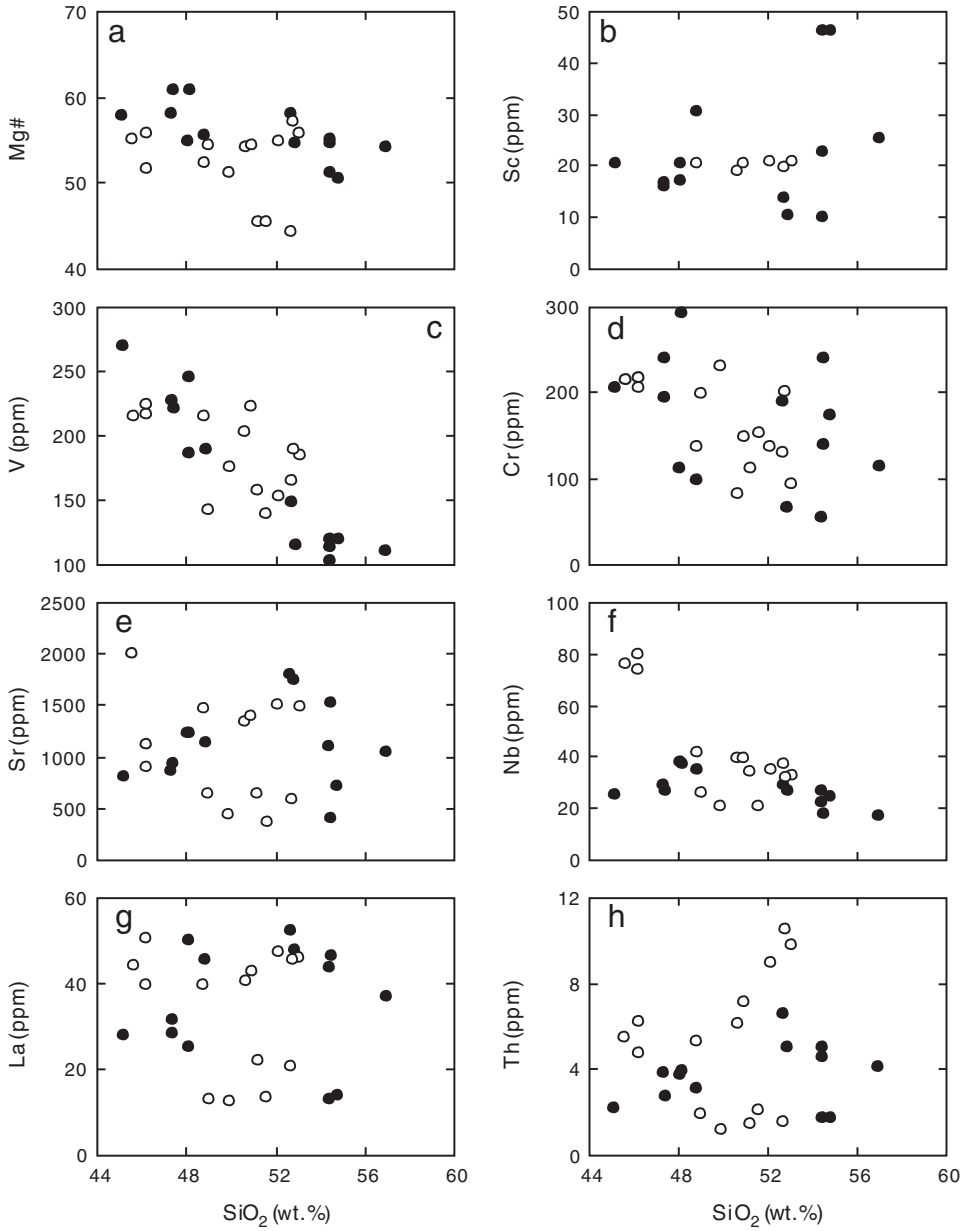

Fig. 6. Mg# and concentrations of selected trace elements versus SiO_2 for the Late Cenozoic alkali basalts, eastern Iran. a. Mg#. b. Sc. c. V. d. Cr. e. Sr. f. Nb. g. La. h. Th. Legend is the same as in Fig. 4.

a feature of the mantle source (Fig. 10a). For the remaining samples, however, the trends directed away from average oceanic basalts towards average crustal values can be explained by minor crustal contamination, or presence of minor crustal components in the mantle source (Fig. 10). In summary, only part of the alkali basalts display minor crustal signatures and the rest of them are largely unaffected.

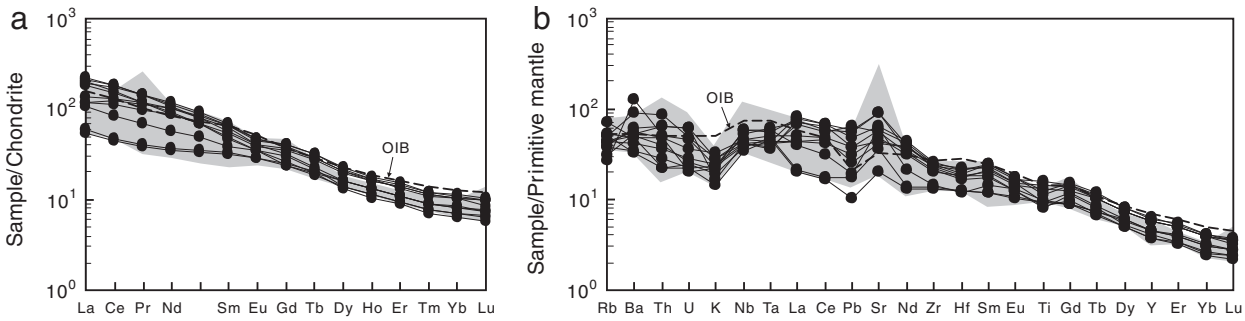

Fig. 7. Chondrite-normalized REE and primitive mantle-normalized trace element variation diagrams for the Late Cenozoic alkali basalts, eastern Iran. Dashed lines denote elemental concentrations for OIB. Gray regions denote data obtained from the same rock suite by Walker et al. (2009). Chondritic values for normalization and OIB data are after Sun and McDonough (1989). Primitive mantle values for normalization are after McDonough and Sun (1995).

Table 3
Rb–Sr and Sm–Nd isotopic data for the Late Cenozoic alkali basalts, eastern Iran.

Sample	Age[a] (Ma)	Rb[b] (ppm)	Sr (ppm)	$^{87}Rb/^{86}Sr$	$^{87}Sr/^{86}Sr$	$\pm2\sigma_m$[c]	$(^{87}Sr/^{86}Sr)_i$[d]	Sm (ppm)	Nd (ppm)	$^{147}Sm/^{144}Nd$	$^{143}Nd/^{144}Nd$	$\pm2\sigma_m$	$(^{143}Nd/^{144}Nd)_i$	εNd (t)
AVNEH	1.60	28.2	1462	0.056	0.704868	0.000011	0.7049	8.54	41.9	0.123	0.512813	0.000004	0.5128	3.4
BVNEH	1.74	27.3	1480	0.053	0.705015	0.000003	0.7050	10.7	51.0	0.127	0.512775	0.000003	0.5128	2.7
CVNEH	4.81	33.0	6192	0.015	0.707253	0.000008	0.7073	8.96	43.8	0.124	0.512768	0.000002	0.5128	2.6
1	2.60	21.7	1514	0.042	0.705113	0.000009	0.7051	8.76	43.5	0.122	0.512775	0.000002	0.5128	2.7
2	2.20	22.7	1341	0.049	0.705545	0.000009	0.7055	9.80	46.1	0.129	0.512800	0.000006	0.5128	3.2
3	2.25	20.5	1389	0.043	0.704954	0.000005	0.7050	10.7	49.3	0.131	0.512823	0.000001	0.5128	3.6
Z-BKH-1	4.20	25.4	1240	0.059	0.704879	0.000002	0.7049	10.0	54.0	0.112	0.512813	0.000002	0.5128	3.5
Z-BKH-2	–	18.6	1738	0.031	0.705896	0.000005	0.7059	7.30	41.9	0.105	0.512793	0.000002	0.5128	3.1
Z-B-1-85	10.1	42.0	870	0.140	0.705020	0.000011	0.7050	9.06	46.6	0.117	0.512779	0.000007	0.5128	2.9
Z-B-2-85	–	26.6	940	0.082	0.704870	0.000012	0.7049	8.09	39.5	0.124	0.512794	0.000004	0.5128	3.1
Z-50-85	11.0	22.7	812	0.081	0.704786	0.000010	0.7048	9.55	46.8	0.123	0.512806	0.000005	0.5128	3.4
08-06	14.3	29.5	404	0.211	0.705453	0.000013	0.7054	4.75	16.1	0.178	0.512706	0.000013	0.5127	1.4
08-06 (dup)											0.512712	0.000004	0.5127	1.5
08-07	–	31.9	721	0.128	0.706524	0.000007	0.7065	4.88	17.1	0.173	0.512718	0.000001	0.5127	1.6
08-112	–	25.7	1144	0.065	0.704747	0.000006	0.7047	9.77	50.4	0.117	0.512795	0.000004	0.5128	3.1
10-08	–	24.0	1098	0.063	0.704737	0.000006	0.7047	7.05	40.1	0.106	0.512787	0.000003	0.5128	3.0
10-10	4.80	29.9	1809	0.048	0.705831	0.000006	0.7058	8.37	48.3	0.105	0.512767	0.000002	0.5128	2.6
10-14	–	16.0	1230	0.038	0.705486	0.000006	0.7055	5.74	26.3	0.132	0.512706	0.000004	0.5127	1.4

[a] Age correction for undated samples is based on ages of samples taken from similar area.
[b] Concentrations of Rb, Sr, Sm and Nd were measured by ICP-MS, $^{87}Rb/^{86}Sr = Rb/Sr \times 2.8956$ and $^{147}Sm/^{144}Nd = Sm/Nd \times 0.60456$.
[c] The 2σ values are the mean standard deviations of the measurements.
[d] $(^{87}Sr/^{86}Sr)_i$ and εNd(t) values were calculated based on an age listed in the first column, $\lambda(^{87}Rb) = 1.42 \times 10^{-11}$ year^{-1}, $\lambda(^{147}Sm) = 6.54 \times 10^{-12}$ year^{-1}, and present day chondritic values of $^{143}Nd/^{144}Nd = 0.512638$, $^{147}Sm/^{144}Nd = 0.1967$, $^{87}Sr/^{86}Sr = 0.7045$ and $^{87}Rb/^{86}Sr = 0.0827$ (Faure and Mensing, 2005).

6.3. Mantle source and partial melting conditions

The low-$(^{87}Sr/^{86}Sr)_i$, high-εNd(t) end of the arrays defined by the data of east Iranian alkali basalts points to a mantle source isotopically comparable to that of several present-day Indian Ocean hotspots (Fig. 8a and b). Likewise, the REE and trace element patterns of the rocks are OIB-like without negative Nb–Ta–Ti anomalies (Fig. 7a and b). Most of them have Zr/Nb that resembles OIB (<10) instead of normal-MORB (~40) and enriched-MORB (~10) (Pearce and Norry, 1979). These characteristics suggest a source in the convecting mantle or in lithospheric mantle not long isolated from it. Late Cenozoic ultrapotassic rocks in Iran, which almost inevitably originated from the lithospheric mantle, possess strong arc-related geochemical signatures (e.g. negative Nb–Ta–Ti anomalies, Ahmadzadeh et al., 2010; Pang et al., 2011) that are not observed in the alkali basalts (Fig. 7b). Further, there lacks clear evidence for residual hornblende or phlogopite, phases suggested being stable only under lithospheric conditions, in the source of the alkali basalts. The strength of negative K anomaly (Fig. 7b) is not correlated with Si_8 or Ti_8 (SiO_2 and TiO_2 concentrations at 8 wt.% MgO after correction by methods of Klein

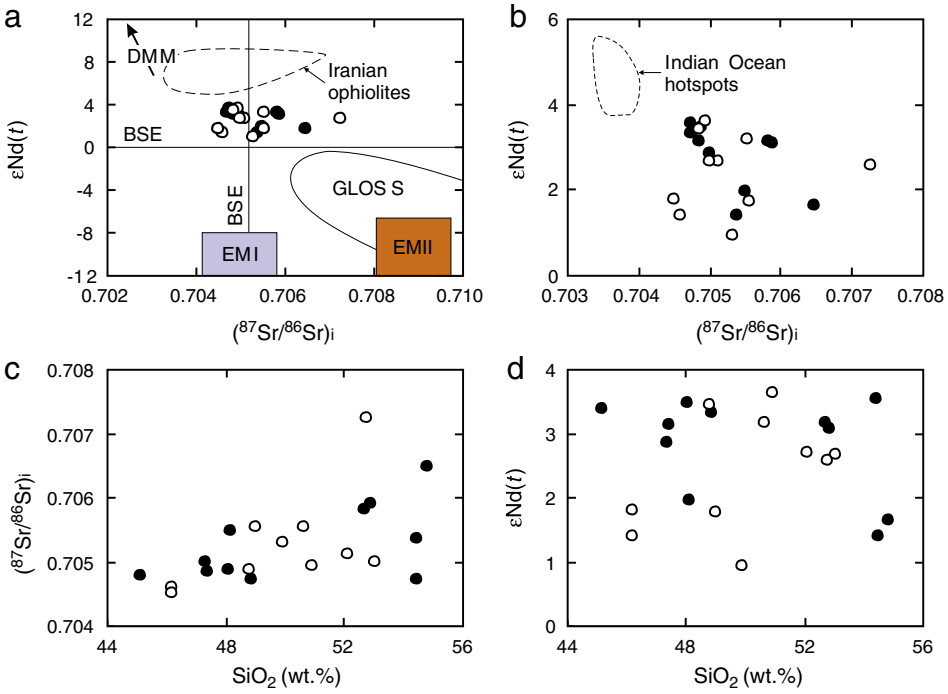

Fig. 8. Binary diagrams involving Sr–Nd isotopes for the Late Cenozoic alkali basalts, eastern Iran. a, b. εNd(t) versus initial Sr isotopic ratios. c. Initial Sr isotopic ratios versus SiO_2. d. εNd(t) versus SiO_2. BSE = Bulk Silicate Earth. Fields of depleted MORB mantle (DMM), enriched mantle I (EMI) and enriched mantle II (EMII) are after Zindler and Hart (1986) and Hofmann (1997). The field of global subducting sediment (GLOSS) are after Plank and Langmuir (1998). Data for Iranian ophiolites are after Zhang et al. (2005). Data for Indian Ocean hotspots are after Sheth et al. (2003), Doucet et al. (2004) and Nohda et al. (2005). Legend is the same as in Fig. 4.

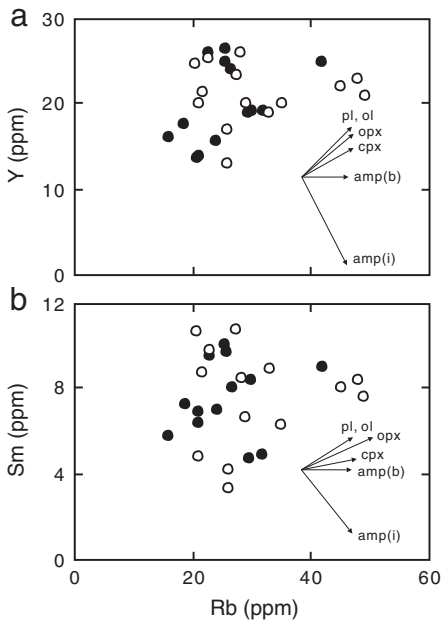

Fig. 9. a. Y–Rb and b. Sm–Rb diagrams for the discrimination between anhydrous and hydrous crystallization for the Late Cenozoic alkali basalts, eastern Iran. Amphibole-bearing crystallizing assemblages should result in negative arrays because of the relatively high amphibole/liquid K_D for Y and Sm. Amphibole-free assemblages should result in positive arrays. Theoretical vectors are after Pearce et al. (1990) and Aldanmaz et al. (2000), and ol = olivine, pl = plagioclase, cpx = clinopyroxene, amp(b) = amphibole in basaltic liquid, amp(i) = amphibole in intermediate liquid. Legend is the same as in Fig. 4.

and Langmuir, 1987), or with the degree of light REE enrichment (e.g. La/Yb) as would be expected for increasing influence of hornblende or phlogopite on magma compositions during mantle melting (Weinstein et al., 2006; Chang et al., 2009; Ma et al., 2011a). Unless the Iranian sub-continental lithospheric mantle is so heterogeneous that is capable of generating ultrapotassic magmas from some domains and alkali basaltic magmas from the others, the asthenosphere is a more plausible source for the alkali basalts.

The degree of partial melting and residual mineralogy in the formation of the east Iranian alkali basalts can be constrained by REE systematics. Strong fractionation between middle and heavy REE of the alkali basalts points to residual garnet in the source because it is almost the only phase in mantle mineralogy capable of fractionating these two sets of elements (Rollinson, 1993; Hauri et al., 1994). To constrain the degree of partial melting, we perform REE modeling on garnet peridotite using the non-modal batch melting equations of Shaw (1970). The results indicate that the alkali basalts could have formed from ~1–5% melting of the primitive mantle or ~3–10% melting of an enriched source (Fig. 11). In the former case, the majority of data cluster at ~1% melting (Fig. 11a) and the ability for such low melt fraction to segregate from the mantle source is uncertain. We are thus in favor of a source that was more REE-rich than the primitive mantle (see later discussion). Further evidence for low degrees of melting is provided by the Sc abundance in the alkali basalts. Scandium is strongly partitioned into garnet and clinopyroxene (Rollinson, 1993); its concentration increases with increasing degrees of melting until there is a harzburgite residue, at which its concentration decreases due to dilution effect. Most east Iranian alkali basalts have Sc contents ranging from 10 to 25 ppm (Fig. 6b), which compares to a range of 35–40 ppm of primitive MORB (Pearce et al., 1990), suggesting that the degrees of melting are in general less than those required to generate MORB. The above interpretations are consistent with melting experiments indicating that alkali basaltic liquids can be generated by relatively low degrees of melting at high pressure of carbonated peridotite (Hirose, 1997) or peridotite–basalt mixtures (Kogiso et al., 1998).

The enriched mantle source inferred for the formation of alkali basalts can be further constrained by trace element and Sr–Nd isotopic geochemistry. Positive $\varepsilon Nd(t)$ coupled with light REE enrichment of the rocks points to a mantle source with long-term light REE depletion, which has only recently become enriched and subsequently melted to form the magmas. Common explanations for such enrichment include: (i) incorporation of small volume melt fractions or subduction-related fluids from the lithospheric mantle (McKenzie, 1989; Anderson, 1994) during passage of asthenosphere-derived magmas, and (ii) migration of volatile-rich fluids or melts released from the subsolidus peridotite shortly before melting (Zou and

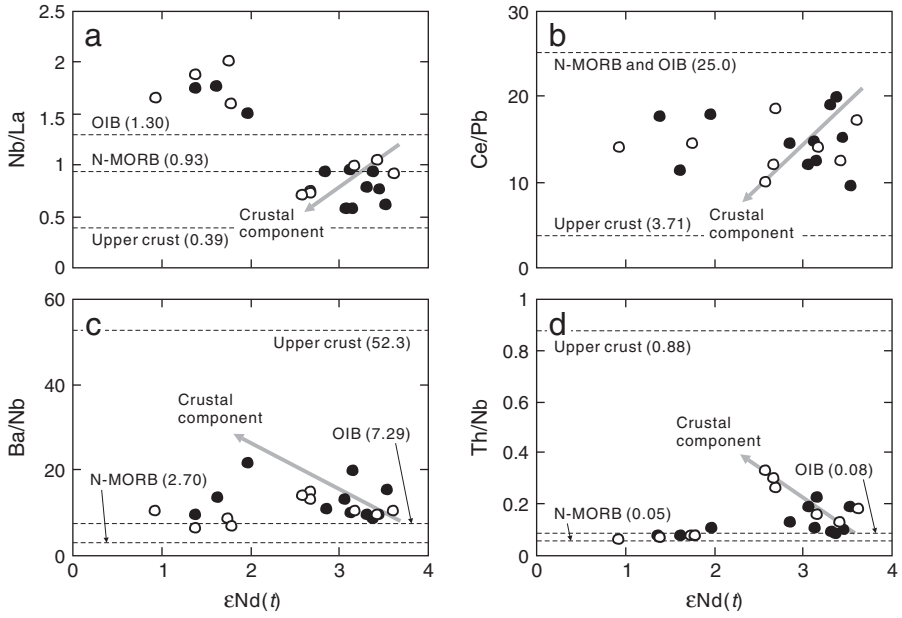

Fig. 10. Binary plots of selected trace element ratios versus $\varepsilon Nd(t)$ for the Late Cenozoic alkali basalts, eastern Iran. a. Nb/La. b. Ce/Pb. c. Ba/Nb. d. Th/Nb. Average values for OIB and MORB are after Sun and McDonough (1989). Average value for upper crust is after Rudnick and Gao (2003). The trends towards low Nb/La and Ce/Pb, and high Ba/Nb and Th/Nb (gray arrows) are indicative of crustal contamination. Legend as in Fig. 4.

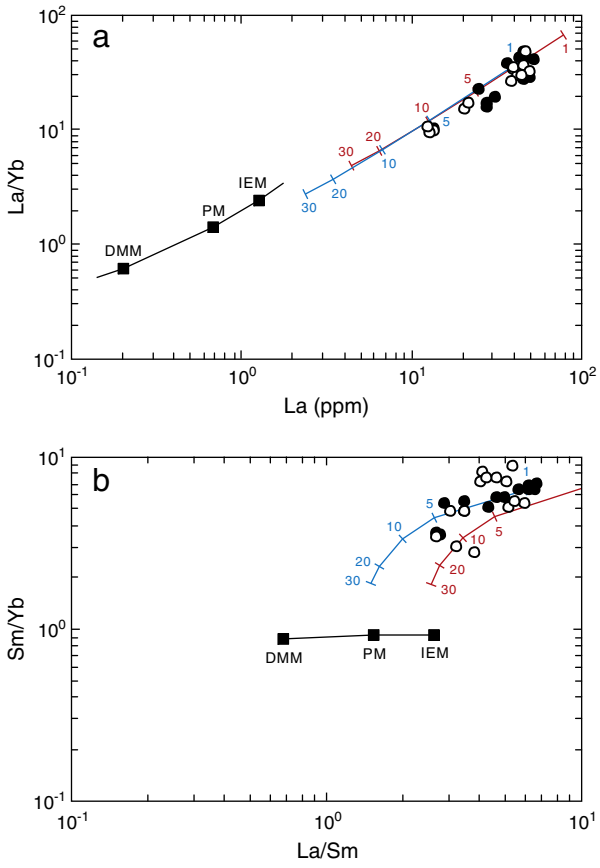

Fig. 11. Modeling of the degree of partial melting for the Late Cenozoic alkali basalts, eastern Iran by co-variation of a. La/Yb and La. b. Sm/Yb and La/Sm. Melting trajectories are calculated using the non-modal batch melting equations of Shaw (1970). The model assumes melting of garnet peridotite with mode and melt mode of $ol_{0.60} + opx_{0.20} + cpx_{0.10} + gt_{0.10}$ and $ol_{0.03} + opx_{0.16} + cpx_{0.88} + gt_{0.09}$, respectively (after Walter, 1998). DMM and primitive mantle (PM) values are after McKenzie and O'Nions (1991) and Sun and McDonough (1989), respectively. Iranian enriched mantle (IEM) is a hypothetical enriched mantle reservoir extrapolated linearly from DMM and PM. Blue and red curves are partial melting trajectories of PM and IEM, respectively; numbers beside the curve denote degrees of melting. Mineral–matrix partition coefficients are from McKenzie and O'Nions (1991). Legend is the same as in Fig. 4.

Zindler, 1996) or from the seismic low velocity zone within the asthenosphere (Niu, 2008; Humphreys and Niu, 2009). The latter possibilities are more reasonable due to the lack of arc-related geochemical features of the alkali basalts as noted above. Hence, we suggest that the enrichment likely took place in the asthenosphere.

6.4. Cause of mantle melting and tectonic implications

Melt generation in the asthenosphere beneath eastern Iran can be achieved by active upwelling of hot asthenosphere (i.e. mantle plumes or localized mantle diapirs) or adiabatic decompression of normal asthenosphere. Mantle plumes are commonly associated with high magma productivity within relatively short periods of geological time (a few m.y.), conditions not applicable to the east Iranian alkali basaltic volcanism. Our results show that the alkali basalts erupted as small volcanic fields for >12 m.y. Further, there is no evidence for regional uplift in the scale of 1000 km or above suggestive of mantle plume impingement (White and McKenzie, 1989; Campbell and Griffiths, 1990). Thus, it is very unlikely that the alkali basaltic volcanism was plume-related, in contrast with that in western Arabia attributed by some authors to the Afar plume (Krienitz et al., 2009). Also, there is no evidence to suggest that localized hotspots are present beneath the Iranian lithosphere. Another possible mechanism for melt generation is by adiabatic decompression of asthenosphere, possibly triggered by rifting and extension (McKenzie and Bickle, 1988), lithospheric thinning (Houseman et al., 1981; Houseman and Molnar, 1997), lithospheric delamination (Bird, 1979) or slab detachment (Davies and von Blanckenburg, 1995). It might be argued that the extension rate in eastern Iran was too low to cause mantle melting without added effect of elevated temperatures (e.g. McKenzie and Bickle, 1988). However, localized stretching associated with movements of the strike–slip faults along which the alkali basalts exposed may help inciting mantle melting (see Aldanmaz et al., 2000). The small scale of the east Iranian alkali basaltic volcanism, its relatively wide areal coverage and long duration are consistent with mechanisms involving adiabetic upwelling and melting.

The Sistan suture zone, eastern Iran marks the collision between the Lut and Afghan continental blocks presumably during the Late Cretaceous (Zarrinkoub et al., 2010). These authors proposed that removal of thickened lithospheric root due to this collisional event caused widespread Eocene–Oligocene calc-alkaline volcanism in the Lut–Sistan region, implying an extensional tectonic regime in eastern Iran at that time. If our petrogenetic model for the alkali basaltic volcanism is correct, this regime most likely continued to exist during Miocene–Quaternary time. Iran is currently undergoing north–south shortening, probably since the Arabia–Eurasia collision (Vernant et al., 2004; Verdel et al., 2011). Chiu et al. (2010) noted a SE-younging trend for the latest subduction-related magmatism along the UDMA, i.e. ~27 Ma in the northern, ~16 Ma in the central and ~7 Ma in the southern part of the arc. This means that the east Iranian alkali basaltic volcanism initiated during the Arabia–Eurasia collision, implying that two distinct tectonic regimes coexist from the Middle Miocene to recent, i.e. extensional in eastern versus compressional in southwestern Iran.

7. Concluding remarks

Widespread but volumetrically minor alkali basaltic volcanism in eastern Iran occurred from ~14 to 1.6 Ma in a post-collisional, intraplate setting. The alkali basalts have OIB-like geochemical signatures and formed by low-degree partial melting of an enriched mantle source in the garnet stability field, presumably in the asthenosphere. They underwent fractionation of olivine, clinopyroxene and Fe–Ti oxides, and minor crustal contamination before eruption. The trigger of volcanism is explained by asthenospheric upwelling caused by delamination of thickened lithospheric root beneath eastern Iran.

Acknowledgments

The authors thank I.-J. Lin and W.-Y. Shao for assistance in ICP-MS analyses. Special thanks are due to Richard Walker for providing samples for Sr–Nd isotopic analyses. Journal reviews by an anonymous reviewer and handling of the manuscript by Editor Donald B. Dingwell are gratefully acknowledged. This study was performed under a joint research program between Birjand University and National Taiwan University, and gained financial support from the National Science Council, Taiwan, ROC.

References

Agard, P., Omrani, J., Jolivet, L., Mouthereau, F., 2005. Convergence history across Zagros (Iran): constraints from collisional and earlier deformation. International Journal of Earth Sciences 94, 401–419.

Ahmadzadeh, G., Jahangiri, A., Lentz, D., Mojtahedi, M., 2010. Petrogenesis of Plio–Quaternary post-collisional ultrapotassic volcanism in NW of Marand, NW Iran. Journal of Asian Earth Sciences 39, 37–50.

Alavi, M., Vaziri, H., Seyed-Emami, K., Lasemi, Y., 1997. The Triassic and associated rocks of the Nakhlak and Aghdarband areas in central and northeastern Iran as remnants of the southern Turanian active continental margin. Geological Society of America Bulletin 109, 1563–1575.

Aldanmaz, E., Pearce, J.A., Thirlwall, M.F., Mitchell, J.G., 2000. Petrogenetic evolution of late Cenozoic, post-collision volcanism in western Anatolia, Turkey. Journal of Volcanology and Geothermal Research 102, 67–95.

Aldanmaz, E., Köprübaşı, N., Gürer, Ö.F., Kaymakçi, N., Gourgaud, A., 2006. Geochemical constraints on the Cenozoic, OIB-type alkaline volcanic rocks of NW Turkey: implications for mantle sources and melting processes. Lithos 86, 50–76.

Allen, M.B., Armstrong, H.A., 2008. Arabia–Eurasia collision and the forcing of mid-Cenozoic global cooling. Palaeogeography, Palaeoclimatology, Palaeoecology 265, 52–58.

Allen, M., Jackson, J., Walker, R., 2004. Late Cenozoic reorganization of the Arabia–Eurasia collision and the comparison of short-term and long-term deformation rates. Tectonics 23, TC2008. doi:10.1029/2003TC001530.

Anderson, D.L., 1994. The sublithospheric mantle as the source of continental flood basalts; the case against the continental lithosphere and plume head reservoirs. Earth and Planetary Science Letters 123, 269–280.

Bird, P., 1979. Continental delamination and the Colorado Plateau. Journal of Geophysical Research 84, 7561–7571.

Camp, V.E., Griffis, R.J., 1982. Character, genesis and tectonic setting of igneous rocks in the Sistan suture zone, eastern Iran. Lithos 15, 221–239.

Campbell, I.H., Griffiths, R.W., 1990. Implications of mantle plume structure for the evolution of flood basalts. Earth and Planetary Science Letters 99, 79–93.

Chang, J.M., Feeley, T.C., Deraps, M.R., 2009. Petrogenesis of basaltic volcanic rocks from the Pribilof Islands, Alaska, by melting of metasomatically enriched depleted lithosphere, crystallization differentiation, and magma mixing. Journal of Petrology 50, 2249–2286.

Chiu, H.-Y., Zarrinkoub, M.H., Chung, S.-L., Lin, I.-J., Yang, H.-M., Lo, C.-H., Mohammadi, S., Khatib, M., 2010. Zircon U–Pb age and geochemical constraints on the magmatic and tectonic evolution in Iran. Abstract to GSA Conference on "Tectonic Crossroads: Evolving Orogens in Eurasia–Africa–Arabia", Oct. 4–8, 2010, p. 520. Ankara, Turkey.

Conrad, G., Montigny, R., Thuizat, R., Westphal, M., 1981. Tertiary and Quaternary geodynamics of southern Lut (Iran) as deduced from palaeomagnetic, isotopic and structural data. Tectonophysics 75, 11–17.

Davies, J.H., von Blanckenburg, F., 1995. Slab breakoff: a model of lithospheric detachment and its test in the magmatism and deformation of collisional orogens. Earth and Planetary Science Letters 129, 85–102.

Doucet, S., Weis, D., Scoates, J.S., Debaille, V., Giret, A., 2004. Geochemical and Hf–Pb–Sr–Nd isotopic constraints on the origin of the Amsterdam–St. Paul (Indian Ocean) hotspot basalts. Earth and Planetary Science Letters 218, 179–195.

Fakhari, M.D., Axen, G.J., Horton, B.K., Hassanzadeh, J., Amini, A., 2008. Revised age of proximal deposits in the Zagros foreland basin and implications for Cenozoic evolution of the High Zagros. Tectonophysics 451, 170–185.

Faure, G., Mensing, T.M., 2005. Isotopes: Principles and Applications. John Wiley and Sons, New Jersey.

Ghazi, A.M., Hassanipak, A.A., Mahoney, J.J., Duncan, R.A., 2004. Geochemical characteristics, ^{40}Ar–^{39}Ar ages and original tectonic setting of the Band-e-Zeyarat/Dar Anar ophiolite, Makran accretionary prism, S.E. Iran. Tectonophysics 393, 175–196.

Hatzfeld, D., Molnar, P., 2010. Comparisons of the kinematics and deep structures of the Zagros and Himalaya and of the Iranian and Tibetan plateaus and geodynamic implications. Reviews of Geophysics 48, RG2005. doi:10.1029/2009RG000304.

Hauri, E.H., Wagner, T.P., Grove, T.L., 1994. Experimental and natural partitioning of Th, U, Pb and other trace elements between garnet, clinopyroxene and basaltic melts. Chemical Geology 117, 149–166.

Hirose, K., 1997. Partial melt compositions of carbonated peridotite at 3 GPa and role of CO_2 in alkali-basalt magma generation. Geophysical Research Letters 24, 2837–2840.

Hoang, N., Flower, M., 1998. Petrogenesis of Cenozoic basalts from Vietnam: implication for origins of a 'diffuse igneous province'. Journal of Petrology 39, 369–395.

Hofmann, A.W., 1997. Mantle geochemistry: the message from oceanic volcanism. Nature 385, 219–229.

Houseman, G.A., Molnar, P.J., 1997. Gravitational (Rayleigh–Taylor) instability of a layer with non-linear viscosity and convective thinning of continental lithosphere. Geophysical Journal International 128, 125–150.

Houseman, G.A., McKenzie, D.P., Molnar, P.J., 1981. Convective instability of a thickened boundary layer and its relevance for the thermal evolution of continental convergent belts. Journal of Geophysical Research 86, 6115–6132.

Humphreys, E.R., Niu, Y., 2009. On the composition of ocean island basalts (OIB): the effects of lithospheric thickness variation and mantle metasomatism. Lithos 112, 118–136.

Irvine, T.N., Baragar, W.R.A., 1971. A guide to the chemical classification of the common volcanic rocks. Canadian Journal of Earth Sciences 8, 448–523.

Jahangiri, A., 2007. Post-collisional Miocene adakitic volcanism in NW Iran: geochemical and geodynamic implications. Journal of Asian Earth Sciences 30, 433–447.

Johnson, J.S., Gibson, S.A., Thompson, R.N., Nowell, G.M., 2005. Volcanism in the Vitim Volcanic Field, Siberia: geochemical evidence for a mantle plume beneath the Baikal Rift Zone. Journal of Petrology 46, 1309–1344.

Jourdan, F., Renne, P.R., 2007. Age calibration of the Fish Canyon sanidine $^{40}Ar/^{39}Ar$ dating standard using primary K–Ar standards. Geochimica et Cosmochimica Acta 71, 387–402.

Jung, D., Keller, J., Khorasani, R., Marcks, C., Baumann, A., Horn, P., 1983. Petrology of the Tertiary magmatic activity in the northern Lut area, east of Iran. Geological Survey of Iran, Report No. 51, pp. 285–336.

Karimpour, M.H., Stern, C.R., Farmer, L., Saadat, S., Malekezadeh, A., 2011. Review of age, Rb–Sr geochemistry and petrogenesis of Jurassic to Quaternary igneous rocks in Lut Block, Eastern Iran. Geopersia 1, 19–36.

Klein, E.M., Langmuir, C.H., 1987. Global correlations of ocean ridge basalt chemistry with axial depth and crustal thickness. Journal of Geophysical Research 92, 8089–8115.

Kogiso, T., Hirose, K., Takahashi, E., 1998. Melting experiments on homogeneous mixtures of peridotite and basalt: application to the genesis of ocean island basalts. Earth and Planetary Science Letters 162, 45–61.

Krienitz, M.-S., Haase, K.M., Mezger, K., van den Bogaard, P., Thiemann, V., Shaikh-Mashail, M.A., 2009. Tectonic events, continental intraplate volcanism, and mantle plume activity in northern Arabia: constraints from geochemistry and Ar–Ar dating of Syrian lavas. Geochemistry, Geophysics, Geosystems 10, Q04008. doi:10.1029/2008GC002254.

Le Bas, M.J., Le Maitre, R.W., Streckeisen, A., Zanettin, B., 1986. A chemical classification of volcanic rocks based on the total alkali–silica diagram. Journal of Petrology 27, 745–750.

Le Maitre, R.W., 2002. Igneous Rocks: A Classification and Glossary of Terms: Recommendations of International Union of Geological Sciences Subcommission on the Systematics of Igneous Rocks. Cambridge University Press, Cambridge.

Lee, H.-Y., Chung, S.-L., Lo, C.-H., Ji, J., Lee, T.-Y., Qian, Q., Zhang, Q., 2009. Eocene Neotethyan slab breakoff in southern Tibet inferred from the Linzizong volcanic record. Tectonophysics 477, 20–35.

Lee, H.-Y., Chung, S.-L., Ji, J., Qian, Q., Gallet, S., Lo, C.-H., Lee, T.-Y., Zhang, Q., 2011. Geochemical and Sr–Nd isotopic constraints on the genesis of the Cenozoic Linzizong volcanic successions, southern Tibet. Journal of Asian Earth Sciences. doi:10.1016/j.jseaes.2011.08.019.

Lo, C.-H., Chung, S.-L., Lee, T.-Y., Wu, G., 2002. Age of the Emeishan flood magmatism and relations to Permian–Triassic boundary events. Earth and Planetary Science Letters 198, 449–458.

Ma, G.S.-K., Malpas, J., Xenophontos, C., Chan, G.H.-N., 2011a. Petrogenesis of latest Miocene–Quaternary continental intraplate volcanism along the northern Dead Sea Fault System (Al Ghab-Homs volcanic field), western Syria: evidence for lithosphere–asthenosphere interaction. Journal of Petrology 52, 401–430.

Ma, G.-S.-K., Malpas, J., Xenophontos, C., Suzuki, K., Lo, C.-H., 2011b. Early Cretaceous volcanism of the Coastal Ranges, NW Syria: magma genesis and regional dynamics. Lithos 126, 290–306.

McDonough, W.F., Sun, S.-S., 1995. The composition of the earth. Chemical Geology 120, 223–253.

McKenzie, D.P., 1989. Some remarks on the movement of small volume melt fractions in the mantle. Earth and Planetary Science Letters 95, 53–72.

McKenzie, D.P., Bickle, M.J., 1988. The volume and composition of melt generated by extension of the lithosphere. Journal of Petrology 29, 627–679.

McKenzie, D., O'Nions, R.K., 1991. Partial melt distributions from inversion of rare earth element concentrations. Journal of Petrology 32, 1021–1091.

McQuarrie, N., Stock, J.M., Verdel, C., Wernicke, B.P., 2003. Cenozoic evolution of Neotethys and implications for the causes of plate motions. Geophysical Research Letters 30, 2036. doi:10.1029/2003GL017992.

Niu, Y., 2008. The origin of alkaline lavas. Science 320, 883–884.

Nohda, S., Kaneoka, I., Hanyu, T., Xu, S., Uto, K., 2005. Systematic variation of Sr-, Nd- and Pb-isotopes with time in lavas of Mauritius, Réunion hotspot. Journal of Petrology 46, 505–522.

Omrani, J., Agard, P., Whitechurch, H., Benoit, M., Prouteau, G., Jolivet, L., 2008. Arc-magmatism and subduction history beneath the Zagros Mountains, Iran: a new report of adakites and geodynamic consequences. Lithos 106, 380–398.

Pang, K.-N., Chung, S.-L., Zarrinkoub, M.H., Chu, C.-H., Lin, I.-J., Lee, H.-Y., 2011. Qal'eh Hasan Ali maars, southeastern Iran: a rare example of Tethyan kamafugitic rocks. Abstract to the 8th Annual Meeting, Asia Oceania Geosciences Society. Aug 8–12, Taipei.

Pearce, J.A., Norry, M.J., 1979. Petrogenetic implications of Ti, Zr, Y, and Nb variations in volcanic rocks. Contributions to Mineralogy and Petrology 69, 33–47.

Pearce, J.A., Bender, J.F., De Long, S.E., Kidd, W.S.F., Low, P.J., Güner, Y., Saroglu, F., Yilmaz, Y., Moorbath, S., Mitchell, J.G., 1990. Genesis of collision volcanism in Eastern Anatolia, Turkey. Journal of Volcanology and Geothermal Research 44, 189–229.

Plank, T., Langmuir, C.H., 1998. The chemical composition of subducting sediment and its consequences for the crust and mantle. Chemical Geology 145, 325–394.

Ramezani, J., Tucker, R.D., 2003. The Saghand region, central Iran: U–Pb geochronology, petrogenesis and implications for Gondwana tectonics. American Journal of Science 303, 622–665.

Rollinson, H.R., 1993. Using Geochemical Data: Evaluation, Presentation, Interpretation. Longman, Singapore.

Rudnick, R.L., Gao, S., 2003. Composition of the continental crust. In: Rudnick, R.L. (Ed.), The Crust, Treatise in Geochemistry, Volume 3. Elsevier-Pergamon, Oxford, pp. 1–64.

Saadat, S., Karimpour, M.H., Stern, C., 2010. Petrochemical characteristics of Neogene and Quaternary alkali olivine basalts from the western margin of the Lut block, Eastern Iran. Iranian Journal of Earth Sciences 2, 87–106.

Saccani, E., Delavari, M., Beccaluva, L., Amini, S., 2010. Petrological and geochemical constraints on the origin of the Nehbandan ophiolitic complex (eastern Iran): Implication for the evolution of the Sistan Ocean. Lithos 117, 209–228.

Şengör, A.M.C., Natal'in, B.A., 1996. Paleotectonics of Asia: fragments of a synthesis. In: Yin, A., Harrison, M. (Eds.), The Tectonic Evolution of Asia. Cambridge University Press, Cambridge, pp. 486–640.

Şengör, A.M.C., Altlner, D., Cin, A., Ustaomer, T., Hsu, K.J., 1988. Origin and assembly of the Tethyside Orogenic Collage at the expense of Gondwana Land. In: Audley-Charles, M.G., Hallam, A.E. (Eds.), Gondwana and Tethys. Geological Society of London Special Publication, Blackwell, Oxford, pp. 119–181.

Shafiei, B., Haschke, M., Shahabpour, J., 2009. Recycling of orogenic arc crust triggers porphyry Cu mineralization in Kerman Cenozoic arc rocks, southeastern Iran. Mineralium Deposita 44, 265–283.

Shaw, D.M., 1970. Trace element fractionation during anatexis. Geochimica et Cosmochimica Acta 34, 237–243.

Sheth, H.C., Mahoney, J.J., Baxter, A.N., 2003. Geochemistry of lavas from Mauritius: mantle source and petrogenesis. International Geology Review 45, 780–797.

Späth, A., Le Roex, A.P., Opiyo-Akech, N., 2001. Plume–lithosphere interaction and the origin of continental rift-related alkaline volcanism — the Chyulu Hills Volcanic Province, southern Kenya. Journal of Petrology 42, 765–787.

Steiger, R.H., Jäger, E., 1977. Subcommission on geochronology: convention on the use of decay constants in geo- and cosmochronology. Earth and Planetary Science Letters 36, 359–362.
Stöcklin, J., 1968. Structural history and tectonics of Iran: a review. American Association of Petroleum Geologists Bulletin 52, 1229–1258.
Sun, S.-S., McDonough, W.F., 1989. Chemical and isotopic systematics in ocean basalt: implication for mantle composition and processes. Magmatism in the Ocean Basins. : In: Saunders, A.D., Norry, M.J. (Eds.), Geological Society of London Special Publications, 42. Blackwell Scientific Publication, Oxford, pp. 313–345.
Tirrul, R., Bell, I.R., Griffis, R.J., Camp, V.E., 1983. The Sistan suture zone of eastern Iran. Geological Society of America Bulletin 94, 134–150.
Verdel, C., Wernicke, B.P., Ramezani, J., Hassanzadeh, J., Renne, P.R., Spell, T.L., 2007. Geology and thermochronology of Tertiary Cordilleran-style metamorphic core complexes in the Saghand region of central Iran. Geological Society of America Bulletin 119, 961–977.
Verdel, C., Wernicke, B.P., Hassanzadeh, J., Guest, B., 2011. A Paleogene extensional arc flare-up in Iran. Tectonics 30, TC3008. doi:10.1029/2010TC002809.
Vernant, P., Nilforoushan, F., Hatzfeld, D., Abbassi, M.R., Vigny, C., Masson, F., Nankali, H., Martinod, J., Ashtiani, A., Bayer, R., Tavakoli, F., Chéry, J., 2004. Present-day crustal deformation and plate kinematics in the Middle East constrained by GPS measurements in Iran and northern Oman. Geophysical Journal International 157, 381–398.
Walker, R., Jackson, J., 2002. Offset and evolution of the Gowk fault, S.E. Iran: a major intra-continental strike–slip system. Journal of Structural Geology 24, 1677–1698.
Walker, R., Gans, P., Allen, M.B., Jackson, J., Khatib, M., Marsh, N., Zarrinkoub, M., 2009. Late Cenozoic volcanism and rates of active faulting in eastern Iran. Geophysical Journal International 177, 783–805.
Walter, M.J., 1998. Melting of garnet peridotite and the origin of komatiite and depleted lithosphere. Journal of Petrology 39, 29–60.
Weinstein, Y., Navon, O., Altherr, R., Stein, M., 2006. The role of lithospheric mantle heterogeneity in the generation of Plio–Pleistocene alkali basaltic suites from NW Harrat Ash Shaam (Israel). Journal of Petrology 47, 1017–1050.
Wellman, H.W., 1966. Active wrench faults of Iran, Afghanistan and Pakistan. Geologische Rundschau 18, 217–234.
White, W.M., McKenzie, D.P., 1989. Magmatism at rift zones: the generation of volcanic continental margins and flood basalts. Journal of Geophysical Research 94, 7685–7729.
Wilson, M., Patterson, R., 2001. Intraplate magmatism related to short-wavelength convective instabilities in the upper mantle: evidence from the Tertiary–Quaternary volcanic province of western and central Europe. In: Ernst, R.E., Buchan, K.L. (Eds.), Mantle Plumes: Their Identification Through Time. : Geological Society of America Special Paper, 352. The Geological Society of America, Inc, Boulder, Colorado, pp. 37–58.
Winchester, J.A., Floyd, P.A., 1977. Geochemical discrimination of different magma series and their differentiation products using immobile elements. Chemical Geology 20, 325–343.
Zarrinkoub, M.H., Chung, S.-L., Chiu, H.-Y., Mohammadi, S., Khatib, M., Lin, I.-J., 2010. Zircon U–Pb age and geochemical constraints from the northern Sistan suture zone on the Neotethyan magmatic and tectonic evolution in eastern Iran. Abstract to GSA Conference on "Tectonic Crossroads: Evolving Orogens in Eurasia–Africa–Arabia", Oct. 4–8, 2010, p. 520. Ankara, Turkey.
Zhang, S.-Q., Mahoney, J.J., Mo, X.-X., Ghazi, A.M., Milani, L., Crawford, A.J., Guo, T.-Y., Zhao, Z.-D., 2005. Evidence for a widespread Tethyan upper mantle with Indian–Ocean-type isotopic characteristics. Journal of Petrology 46, 829–858.
Zindler, A., Hart, S., 1986. Chemical geodynamics. Annual Review of Earth and Planetary Sciences 14, 493–571.
Zou, H., Zindler, A., 1996. Constraints on the degree of dynamic partial melting and source composition using concentration ratios in magmas. Geochimica et Cosmochimica Acta 60, 711–717.